The Astrophysical Journal Letters, 997:L10 (24pp), 2026 January 20 https://doi.org/10.3847/2041-8213/ae2910

The Most Luminous Known Fast Blue Optical Transient AT 2024wpp: Unprecedented Evolution and Properties in the Ultraviolet to the Near-infrared

Natalie LeBaron[1,2], Raffaella Margutti[1,2,3], Ryan Chornock[1,2], Nayana A. J.[1,2], Olivia Aspegren[1], Wenbin Lu[1,2,4], Brian D. Metzger[5,6], Daniel Kasen[1,2,3,7], Thomas G. Brink[1], Sergio Campana[8], Paolo D'Avanzo[8], Jakob T. Faber[9], Matteo Ferro[8,10], Alexei V. Filippenko[1], Ryan J. Foley[11], Xinze Guo[1], Erica Hammerstein[1], Saurabh W. Jha[12], Charles D. Kilpatrick[13], Giulia Migliori[14], Dan Milisavljevic[15,16], Kishore C. Patra[11], Huei Sears[12], Jonathan J. Swift[17], Samaporn Tinyanont[18], Vikram Ravi[9,19], Yuhan Yao[1,2,20], Kate D. Alexander[21], Prasiddha Arunachalam[11], Edo Berger[22], Joe S. Bright[23,24], Chuck Cynamon[25], Kyle W. Davis[11], Braden Garretson[15], Puragra Guhathakurta[11], Wynn V. Jacobson-Galán[9], D. O. Jones[26], Ravjit Kaur[11], Stefan Kimura[27], Tanmoy Laskar[28,29], Morgan Nuñez[30], Michaela Schwab[12], Monika D. Soraisam[26], Nao Suzuki[31,32], Kirsty Taggart[11], Eli Wiston[1,2], Yi Yang[33], and WeiKang Zheng[1]

[1] Department of Astronomy, University of California, Berkeley, CA 94720-3411, USA
[2] Berkeley Center for Multi-messenger Research on Astrophysical Transients and Outreach (Multi-RAPTOR), University of California, Berkeley, CA 94720-3411, USA
[3] Department of Physics, University of California, 366 Physics North MC 7300, Berkeley, CA 94720, USA
[4] Theoretical Astrophysics Center, UC Berkeley, Berkeley, CA 94720, USA
[5] Department of Physics and Columbia Astrophysics Laboratory, Columbia University, New York, NY 10027, USA
[6] Center for Computational Astrophysics, Flatiron Institute, 162 5th Avenue, New York, NY 10010, USA
[7] Nuclear Science Division, Lawrence Berkeley National Laboratory, 1 Cyclotron Road, Berkeley, CA 94720, USA
[8] INAF—Osservatorio Astronomico di Brera, Via Bianchi 46, I-23807 Merate (LC), Italy
[9] Cahill Center for Astronomy and Astrophysics, MC 249-17 California Institute of Technology, Pasadena CA 91125, USA
[10] Università degli Studi dell'Insubria, Dipartimento di Scienza e Alta Tecnologia, Via Valleggio 11, 22100 Como, Italy
[11] Department of Astronomy and Astrophysics, University of California, Santa Cruz, CA 95064, USA
[12] Department of Physics and Astronomy, Rutgers, the State University of New Jersey, 136 Frelinghuysen Road, Piscataway, NJ 08854-8019, USA
[13] Center for Interdisciplinary Exploration and Research in Astrophysics (CIERA) and Department of Physics and Astronomy, Northwestern University, Evanston, IL 60208, USA
[14] INAF Istituto di Radioastronomia, via Gobetti 101, 40129 Bologna, Italy
[15] Department of Physics and Astronomy, Purdue University, 525 Northwestern Avenue, West Lafayette, IN 47907, USA
[16] Institute of Physical Artificial Intelligence, Purdue University, West Lafayette, IN 47907, USA
[17] The Thacher School, 5025 Thacher Road, Ojai, CA 93023, USA
[18] National Astronomical Research Institute of Thailand, 260 Moo 4, Donkaew, Maerim, Chiang Mai, 50180, Thailand
[19] Owens Valley Radio Observatory, California Institute of Technology, Big Pine, CA 93513, USA
[20] Miller Institute for Basic Research in Science, 206B Stanley Hall, Berkeley, CA 94720, USA
[21] Department of Astronomy/Steward Observatory, 933 North Cherry Avenue, Room N204, Tucson, AZ 85721-0065, USA
[22] Center for Astrophysics | Harvard & Smithsonian, 60 Garden Street, Cambridge, MA 02138-1516, USA
[23] Astrophysics, Department of Physics, University of Oxford, Keble Road, Oxford OX1 3RH, UK
[24] Breakthrough Listen, Astrophysics, Department of Physics, University of Oxford, Keble Road, Oxford OX1 3RH, UK
[25] Supra Solem Observatory, Santa Lucia Mountains, CA, USA
[26] Gemini Observatory, NSF's NOIRLab, 670 N. A'ohoku Place, Hilo, HI 96720, USA
[27] Physics Department, Willamette University, Salem, OR, USA
[28] Department of Physics & Astronomy, University of Utah, Salt Lake City, UT 84112, USA
[29] Department of Astrophysics/IMAPP, Radboud University, P.O. Box 9010, 6500 GL, Nijmegen, The Netherlands
[30] Department of Physics & Astronomy, San Francisco State University, San Francisco, CA 94132, USA
[31] E.O. Lawrence Berkeley National Laboratory, 1 Cyclotron Road, Berkeley, CA 94720, USA
[32] Department of Physics, Florida State University, 77 Chieftan Way, Tallahassee, FL 32306, USA
[33] Department of Physics, Tsinghua University, Qinghua Yuan, Beijing 100084, People's Republic of China
Received 2025 August 29; revised 2025 November 10; accepted 2025 December 6; published 2026 January 13

Abstract

We present an extensive photometric and spectroscopic ultraviolet–optical–infrared campaign on the luminous fast blue optical transient (LFBOT) AT 2024wpp over the first ∼100 days. AT 2024wpp is the most luminous LFBOT discovered to date, with $L_{\rm pk} \approx (2\text{–}4) \times 10^{45}$ erg s^{-1} (5–10 times that of the prototypical AT 2018cow). This extreme luminosity enabled the acquisition of the most detailed LFBOT UV light curve thus far. In the first ∼45 days, AT 2024wpp radiated $>10^{51}$ erg, surpassing AT 2018cow by an order of magnitude and requiring a power source beyond the radioactive ^{56}Ni decay of traditional supernovae. Like AT 2018cow, the UV–optical spectrum of AT 2024wpp is dominated by a persistently blue thermal continuum throughout our monitoring, with blackbody parameters at a peak of $T > 30{,}000$ K and $R_{\rm BB}/t \approx 0.2c$–$0.3c$. We find evidence for cooling until ∼10 days; thereafter, $T \gtrsim 20{,}000$ K is maintained. We interpret the featureless spectra as a consequence of continuous energy injection from a central source of high-energy emission that maintains high ejecta ionization.

After 35 days, faint (equivalent width (EW) $\lesssim$ 10 Å) H and He spectral features with kinematically separate velocity components centered at 0 and $-6400\,\mathrm{km\,s^{-1}}$ emerge, implying spherical symmetry deviations. A near-infrared excess of emission above the optical blackbody emerges between 20 and 30 days, with a power-law spectrum $F_{\nu,\mathrm{NIR}} \propto \nu^{-0.3}$ at 30 days. We interpret this distinct emission component as either reprocessing of early UV emission in a dust echo or free–free emission in an extended medium above the optical photosphere. LFBOT asphericity and multiple outflow components (including mildly relativistic ejecta), together with the large radiated energy, are naturally realized by super-Eddington accretion disks around neutron stars or black holes and their outflows.

Unified Astronomy Thesaurus concepts: Transient sources (1851); High energy astrophysics (739)

1. Introduction

Recently, high-cadence, wide-field optical transient surveys have led to the identification of a new class of astrophysical phenomena, fast blue optical transients (FBOTs). Characterized by an extremely rapid rise to maximum light ($t_{\mathrm{rise}} \lesssim 10$ days), luminous emission that can reach $L_{\mathrm{pk}} > 10^{45}\,\mathrm{erg\,s^{-1}}$, and persistent blue colors for weeks after peak (M. R. Drout et al. 2014; I. Arcavi et al. 2016; M. Tanaka et al. 2016; S. J. Prentice et al. 2018; M. Pursiainen et al. 2018; A. Rest et al. 2018; A. Y. Q. Ho et al. 2023b; M. Nicholl et al. 2023), these transients challenge traditional supernova (SN) models that are powered by the radioactive decay of ^{56}Ni. Alternative sources of energy are therefore needed. Proposed sources include shock interaction with dense circumstellar material (CSM; e.g., B. Margalit 2022; C. Pellegrino et al. 2022; D. K. Khatami & D. N. Kasen 2024) and a central engine powered by either magnetar spin-down or accretion onto a compact object. There is debate on the nature of the compact object, as well as (in the latter case) on the origin of the accreted material. Considered models include magnetar-powered SNe (S. J. Prentice et al. 2018; I. Vurm & B. D. Metzger 2021), accretion onto a compact object at the center of a failed SN (R. Margutti et al. 2019; E. Quataert et al. 2019), merger of a black hole (BH) and Wolf–Rayet (W-R) star (B. D. Metzger 2022a), tidal disruption event (TDE) of a main-sequence companion star by a stellar-mass BH or neutron star (NS; D. Tsuna & W. Lu 2025), and TDE by an intermediate-mass BH (IMBH; i.e., $\gtrsim 10^3\,M_\odot$; D. A. Perley et al. 2019; C. P. Gutiérrez et al. 2024; A. Y. Q. Ho et al. 2023a).

FBOTs span a wide range of peak luminosities ($L_{\mathrm{pk}} \approx 10^{42}$–$10^{45}\,\mathrm{erg\,s^{-1}}$; e.g., A. Y. Q. Ho et al. 2023b), are not intrinsically rare (7%–11% of the core-collapse SN (CCSN) rate; M. R. Drout et al. 2014; A. Y. Q. Ho et al. 2023b), and are likely a heterogeneous class. Lower-luminosity ($L_{\mathrm{pk}} \lesssim 10^{43}\,\mathrm{erg\,s^{-1}}$) FBOTs likely represent manifestations of the fast-evolving tail of hydrogen-poor SNe (e.g., A. Y. Q. Ho et al. 2023b) possibly powered by shock interaction (and subsequent shock-cooling emission) between their fast ejecta and surrounding CSM. However, there is a subset of FBOTs with $L_{\mathrm{pk}} > 10^{43}\,\mathrm{erg\,s^{-1}}$ that are also associated with luminous radio and/or X-ray emission. These luminous FBOTs (LFBOTs; also called "cow-like" transients after the prototypical AT 2018cow) are much rarer (<1% the CCSN rate; D. L. Coppejans et al. 2020; A. Y. Q. Ho et al. 2023b) and thus either represent the outcome of a more unusual stellar evolution pathway (e.g., D. Tsuna & W. Lu 2025) or might not be stellar explosions at all (e.g., B. D. Metzger 2022a). Their persistent blue colors (indicative of high temperatures $>10^4$ K) and featureless ultraviolet (UV)–optical–near-infrared (NIR) spectra over many weeks point to the presence of a central heating source that is distinct from the outer shock CSM interaction. From this perspective LFBOTs present clear observational analogies to the recently identified class of featureless TDEs (E. Hammerstein et al. 2023; Y. Yao et al. 2023), which may also extend to the underlying physics of these phenomena. Other engine-driven explosions with mildly relativistic ejecta include the EP 250108a/SN 2025kg–like sample of fast X-ray transients that eventually showed broad-lined Type Ic SN (SN Ic) spectral features (S. Campana et al. 2006; E. Pian et al. 2006; A. M. Soderberg et al. 2006; R. A. J. Eyles-Ferris et al. 2025; J. C. Rastinejad et al. 2025; G. P. Srinivasaragavan et al. 2025; H. Sun et al. 2025; J. N. D. van Dalen et al. 2025). These transients have been noted for their similarities to LFBOTs in both optical evolution (including detection of Hα for EP 250108a/SN 2025kg; J. C. Rastinejad et al. 2025) and X-ray emission, though there seems to be a more robust physical link between these transients and gamma-ray bursts–SNe than LFBOTs.

Identified LFBOTs accompanied with X-ray/radio emission include AT 2018cow (S. J. Prentice et al. 2018; A. Y. Q. Ho et al. 2019; R. Margutti et al. 2019; D. A. Perley et al. 2019; Y. Chen et al. 2023a), AT 2018lug (ZTF18abvkwla, the "Koala"; A. Y. Q. Ho et al. 2020), AT 2020mrf (Y. Yao et al. 2022), AT 2022tsd (A. Y. Q. Ho et al. 2023a; D. Matthews et al. 2023), CRTS-CSS161010 J045834–081803 (CSS161010; D. L. Coppejans et al. 2020; C. P. Gutiérrez et al. 2024), AT 2020xnd (D. A. Perley et al. 2021; J. S. Bright et al. 2022; A. Y. Q. Ho et al. 2022), AT 2023fhn (A. A. Chrimes et al. 2024a, 2024b), AT 2024qfm (M. Fulton et al. 2024), and AT 2024wpp (E. O. Ofek et al. 2025; M. Pursiainen et al. 2025). From this small sample of objects, LFBOTs are inferred to possess aspherical ejecta with outflows that have high velocity near the poles ($\sim 0.2c$) and lower velocity at the equator (few $\times$ 10^3 km s^{-1}). At early times ($\lesssim$15–30 days), the ejecta reprocess X-rays produced by the central engine into UV–optical–IR (UVOIR) wavelengths (e.g., A. L. Piro & W. Lu 2020; K. Uno & K. Maeda 2020; D. Calderón et al. 2021; C. Chen & R.-F. Shen 2022). As the ejecta photosphere recedes, H and He features are revealed in their spectra. While such observational features of this class are well established, the exact ejecta structure and intrinsic nature of LFBOTs are unconstrained owing to the lack of objects with extensive UV–NIR pre-to-post-peak photometry and spectroscopy. Only two previous LFBOTs (AT 2018cow and CSS161010) have extensive, multiepoch optical spectral sequences. AT 2024wpp presents a rare opportunity to obtain this dataset.

AT 2024wpp is the most luminous LFBOT discovered to date (both in the UV and bolometrically); the first to have pre-peak UV photometry, which led to an extensive UV–optical observational campaign; the second to be sampled in the NIR photometrically and spectroscopically, which revealed the second detected LFBOT NIR excess; the second to be observed with optical polarimetry (M. Pursiainen et al. 2025); and only the third with an optical spectral sequence

up to 55 days (rest frame), which revealed unprecedented line profiles of H and He. Despite being more distant (411 Mpc) than the closest known LFBOT AT 2018cow (60 Mpc), the extreme luminosity of AT 2024wpp ultimately enabled this well-sampled dataset and allowed for the search for short-duration optical flares like those observed in AT 2022tsd (A. Y. Q. Ho et al. 2023a), which were not detected (E. O. Ofek et al. 2025). Here in Paper I we present our multiwavelength observations of AT 2024wpp over the first ∼100 days of evolution, with focus on the transient thermal UVOIR emission. We analyze the broadband X-ray and radio emission from AT 2024wpp in our companion paper (A. J. Nayana et al. 2025 hereafter Paper II). We refer to the results from Paper II where appropriate to build a holistic picture of the event.

This paper is structured as follows: We present our UV, optical, and NIR observations (photometry and spectroscopy) in Section 2 and derive the bolometric luminosity of the transient in Section 3. In Section 4, we discuss the astrophysical implications of the observed featureless spectra maintained for weeks after discovery and the later emergence of H+He emission lines with unusual profiles. Section 6 explores the nature of the NIR excess in the context of free–free emission and dust models. We discuss in Section 7 AT 2024wpp in the context of other LFBOTs and TDEs with similar spectral features, and we conclude in Section 8.

2. Observations

From D. A. Perley et al. (2024), AT 2024wpp is located at redshift $z = 0.0868$, which corresponds to a luminosity distance of 411 Mpc under ΛCDM cosmological parameters $H_0 = 67.4\,\mathrm{km\,s^{-1}\,Mpc^{-1}}$, $\Omega_m = 0.315$, and $\Omega_\Lambda = 0.685$ (Planck Collaboration et al. 2020). We estimate the time of first light to be MJD = 60578.3. We refer to times with respect to this t_0, in the observed reference frame, and as UTC unless otherwise stated. Uncertainties in t_0 have no impact on our major conclusions. Uncertainties are reported at the 1σ (Gaussian equivalent) confidence level, and upper limits correspond to a 3σ statistical level. We correct for Milky Way (MW) reddening using $R_V = 3.1$ adopting the E. L. Fitzpatrick (1999) model with $A_V = 0.078$ mag and $E(B-V) = 0.025$ mag. Other than for the Swift UV photometry discussed in Section 2, we assume that host galaxy extinction is negligible and do not apply a correction because of the large transient separation from its host (3.″1; D. A. Perley et al. 2024) and the lack of narrow absorption lines in the early-time, high signal-to-noise ratio (S/N) spectra.

2.1. UV–NIR Photometry

Observations with the Ultra-Violet/Optical Telescope (UVOT; P. W. A. Roming et al. 2005) on board the Neil Gehrels Swift Observatory (N. Gehrels et al. 2004) began on 2024 September 27 at 9:52:34 ($\delta t = 2.1$ days; PI M. Coughlin). An extensive 1-day cadence UVOT campaign was initiated under our Guest Observer program (PI R. Margutti) and covered the period $\delta t = 5$–59 days, followed by a lower-cadence campaign to sample the later-time evolution of AT 2024wpp until $\delta t = 119$ days. This prompt and intense monitoring led to the acquisition of the first UV data during the rise time of an FBOT and to the most detailed UV data on an FBOT to date.

Ground-based optical and NIR photometry of AT 2024wpp was obtained between 2024 October 2 and 2024 October 25 ($\delta t = 7$–30 days). Photometry in filters g, r, and i was obtained from the Las Cumbres Observatory (LCO) Global Telescope Network 1 m telescopes[34] and the Supra Solem Observatory operating in SkiesAway Remote Observatory with a Plane-Wave CDK 125 telescope. Additional g-, r-, and i-band photometry, as well as three epochs of z-band photometry, was obtained from the Thacher 0.7 m telescope in Ojai, CA (J. J. Swift et al. 2022). Three epochs of optical and NIR observations in filters g, r, i, J, and H (epoch 1); g, r, i, and J (epoch 2); and J (epoch 3) were obtained by the 0.6 m robotic Rapid Eye Mount telescope (REM; R. M. Zerbi et al. 2001; S. Covino et al. 2004), located at the European Southern Observatory (ESO) at La Silla (Chile). A fading source was detected consistent with the transient position in all REM optical observations; however, no infrared counterpart was detected in any of the three REM NIR observations. An additional four epochs of NIR imaging were obtained with the Flamingos-2 instrument (S. S. Eikenberry et al. 2004; S. Eikenberry et al. 2012) mounted on the Gemini-South Telescope. The first three Gemini epochs are derived from the acquisition images for NIR spectroscopy in the J and H bands; the fourth epoch was observed in J, H, and K_s. The source was detected at all Gemini epochs.

We also collected publicly available photometry from the Transient Name Server[35] (TNS) AstroNotes and the Asteroid Terrestrial-impact Last Alert System (ATLAS; J. L. Tonry et al. 2018; K. W. Smith et al. 2020). ATLAS data were obtained through the ATLAS forced-photometry server.[36] All ground-based optical photometry is listed in Table B1, including the public Zwicky Transient Facility (ZTF) photometry reported to TNS (A. Y. Q. Ho et al. 2024). Magnitudes in this table are corrected for MW extinction.

All data were reduced using standard procedures. Swift UVOT observations span the wavelength range from $\lambda_c = 1928$ Å ($w2$ filter) to $\lambda_c = 5468$ Å (V filter; central wavelengths listed). We extracted the UVOT photometry following standard practice and updated zero-points (e.g., P. J. Brown et al. 2009). Specifically, we used a 5″-radius source region centered at the location of AT 2024wpp and a 35″-radius source-free region to estimate the background contribution. We merged individual exposures to reach a minimum S/N $\gtrsim$ 10. We estimate the host galaxy flux contribution to be negligible at early times ($\delta t < 45$ days) for all filters. Final observations in filters $w1$ and $w2$ near 100 days are assumed to be host dominated, and we use these measurements to host-correct the $w1$ and $w2$ data. Pre-explosion observations from the Galaxy Evolution Explorer (GALEX; D. C. Martin et al. 2005) measured the host galaxy UV emission to be $m_{\mathrm{NUV}} = 22.00 \pm 0.48$ mag. The GALEX NUV to Swift $m2$ filter correction based on the best-fitting host galaxy spectral energy distribution (SED) from BLAST[37] is $\delta_{\mathrm{mag}} \approx 0.016$ mag. We thus use the filter-corrected GALEX NUV measurement (with added 5% systematic uncertainty to account for filter transmission differences) to correct for the host contribution to the $m2$ Swift observations. Swift UVOT

[34] https://lco.global/
[35] https://www.wis-tns.org/object/2024wpp
[36] https://fallingstar-data.com/forcedphot/
[37] https://blast.scimma.org/transients/2024wpp/

photometry (with correction for MW extinction but without host correction) is listed in Table B2.

Supra Solem images were flat-fielded, bias-corrected, and dark-corrected using Maxim DL processes,[38] implemented automatically by the ACP Observatory Control Software.[39] Template subtraction was performed on the science images with the High Order Transform of Psf ANd Template Subtraction (HOTPANTS; A. Becker 2015) code with pre-explosion Pan-STARRS images. Aperture photometry was performed on the subtracted images using the `photutils` package in `astropy` (Astropy Collaboration et al. 2013) and flux-calibrated from zero-points derived from Pan-STARRS DR2 sources (H. Flewelling 2018).

For the LCO photometry, calibrated BANZAI frames were downloaded from the LCO archive and aperture photometry was performed using the procedure outlined above for Supra Solem Observatory data.

REM data reduction was performed with the REM reduction pipeline. After bias subtraction, nonuniformities were corrected using a normalized flat-field frame processed with tools from the Swift Reduction Package (SRP).[40] NIR data were sky-subtracted using the median of individual frames. Frame registration was performed using the Python-based software Astroalign (M. Beroiz et al. 2020), and astrometric solutions were derived against Gaia DR3 stars (Gaia Collaboration et al. 2023). Aperture photometry was performed, calibrating against Pan-STARRS DR2 sources (PS1; H. Flewelling 2018). Upper limits on the NIR photometry were derived using calibration against Two Micron All Sky Survey (2MASS) stars (M. F. Skrutskie et al. 2006).

Flamingos-2 images were reduced with standard recipes in DRAGONS (K. Labrie et al. 2023a, 2023b). Aperture photometry was performed with `photutils`, and flux calibration was done using zero-points derived from 2MASS stars. The MW extinction-corrected NIR photometry from Gemini and REM is listed in Table B3.

Thacher *griz* images were processed using standard reduction procedures using `photpipe` (A. Rest et al. 2005). All images were calibrated using flat-field and bias frames from the same night and instrumental configuration and astrometrically calibrated to Gaia DR3 calibrators. We transformed each image to a regular image coordinate frame with `SWarp` (E. Bertin 2010) and then performed point-spread function (PSF) photometry using `DoPhot` (P. L. Schechter et al. 1993). Finally, we photometrically calibrated photometry from each field using Pan-STARRS DR2 sources.

All photometric observations are presented in Figure 1.

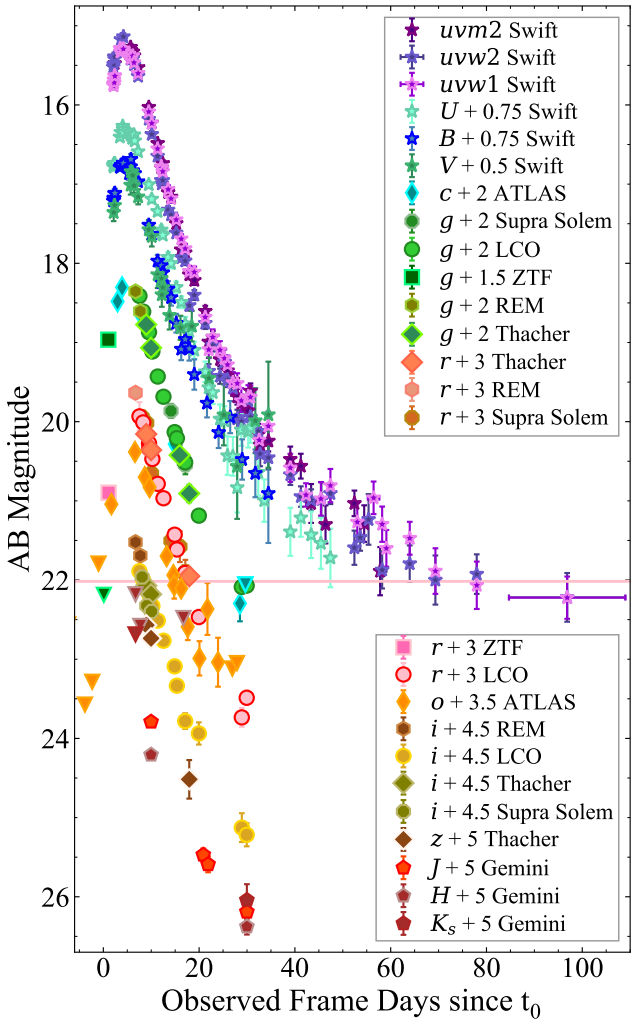

Figure 1. UVOIR light curve of AT 2024wpp corrected for Galactic extinction. Offsets are applied for clarity. Pink horizontal line: pre-transient GALEX NUV emission at the location of the transient, marking the level of UV emission from the host galaxy. At $\gtrsim$80 days, the Swift UV photometry is dominated by the host galaxy flux. In Section 2.1, we use the GALEX NUV observation to subtract the host galaxy contribution from the Swift *m*2 photometry. Magnitudes are expressed in the AB system (J. B. Oke & J. E. Gunn 1983).

2.2. Optical and NIR Spectroscopy

To estimate our t_0, we linearly extrapolate the rise rate in flux between the first ZTF *g*-band marginal detection and the subsequent detection (A. Y. Q. Ho et al. 2024).

We present 16 optical spectra of AT 2024wpp observed 4–63 days from explosion in Figure 2. We list these spectra in Table B4 and overview reduction details below. Data files for these spectra are available at WISeREP (O. Yaron & A. Gal-Yam 2012).[41]

We obtained seven optical spectra with the Kast double spectrograph (J. S. Miller & R. Stone 1994) mounted on the Shane 3 m telescope with a 2.″0-wide slit. Three of these Kast spectra were reduced using the `UCSC Spectral Pipeline`[42] (M. R. Siebert et al. 2020), a custom data reduction pipeline based on procedures outlined by R. J. Foley et al. (2003) and J. M. Silverman et al. (2012, and references therein), while the other Kast spectra were reduced in an equivalent manner. The two-dimensional spectra were bias-corrected, flat-field-corrected, adjusted for varying gains across different chips and amplifiers, and trimmed. One-dimensional spectra were extracted using the optimal algorithm (K. Horne 1986). The spectra were wavelength-calibrated using internal comparison-lamp spectra with linear shifts applied by cross-correlating the observed night-sky lines in each spectrum to a master night-sky spectrum. Flux calibration and telluric correction were performed using standard stars at a similar air mass to that of

[38] https://cdn.diffractionlimited.com/help/maximdl/MaxIm-DL.htm
[39] http://scheduler.dc3.com/
[40] http://www.me.oa-brera.inaf.it/utenti/covino/usermanual.html
[41] https://www.wiserep.org/object/26437
[42] https://github.com/msiebert1/UCSC_spectral_pipeline

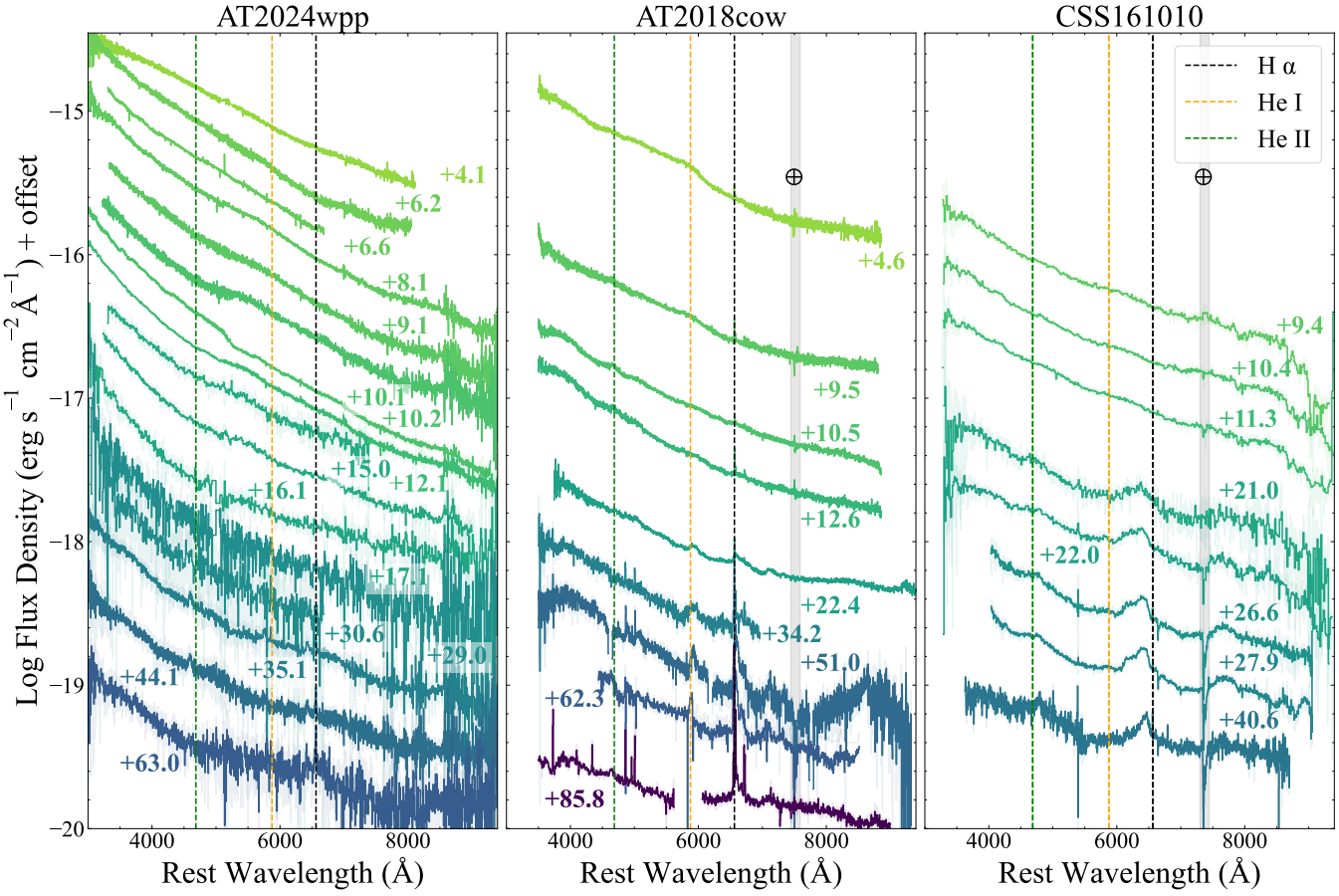

Figure 2. Left: collated AT 2024wpp optical spectral series spanning from +4.1 to +63.0 days from t_0 (observed frame). Spectra are plotted in the rest frame and are binned for visual clarity (native binning is shown in lighter shading). For comparison, coeval optical spectra of the only other well-sampled LFBOTs, AT 2018cow (R. Margutti et al. 2019) and CSS161010 (C. P. Gutiérrez et al. 2024), are plotted in the middle and right panels, respectively, and identified by the observed-frame epoch of observation. We note that the +4.1-day AT 2024wpp spectrum has an unreliable spectral slope.

the science exposures. We combine the sides by scaling one spectrum to match the flux of the other in the overlap region and use their error spectra to correctly weight the spectra when combining. More details of this process are discussed elsewhere (R. J. Foley et al. 2003; J. M. Silverman et al. 2012; M. R. Siebert et al. 2020). The +4.1-day Kast spectrum was obtained at air mass 1.7 with the slit oriented 20°–30° away from the parallactic angle (A. V. Filippenko 1982), so this spectrum experienced enhanced loss of blue light, making the blue spectral slope unreliable.

We also obtained five optical spectra with LRIS (J. B. Oke et al. 1995) mounted on the Keck I 10 m telescope. LRIS spectra were reduced and calibrated similarly to the Kast spectra. Low-order polynomial fits to calibration-lamp spectra were used to establish the wavelength scale, and small adjustments derived from night-sky lines in the object frames were applied. The +12.1-day LRIS spectrum was reduced in an equivalent manner with LPipe (D. A. Perley 2019). LRIS is equipped with an atmospheric dispersion corrector, thereby precluding differential slit losses.

We obtained two optical spectra of AT 2024wpp with the Southern African Large Telescope (SALT) Robert Stobie Spectrograph (RSS; M. P. Smith et al. 2006). The first observation was taken on 2024 October 10, and the second was taken on 2024 October 25. We used a 1.″5-wide slit and the PG0900 grating in two tilt positions to cover the blue part of the spectrum without detector chip gaps. The data were reduced using RUSALT, a custom pipeline based on PySALT (S. M. Crawford et al. 2010) that uses standard Pyraf (Science Software Branch at STScI 2012) spectral reduction routines such as wavelength and relative flux calibration, one-dimensional extraction, and the removal of cosmic rays and telluric absorption.

We obtained an optical spectrum of AT 2024wpp using the DeVeny optical spectrograph mounted on the 4.3 m Lowell Discovery Telescope (LDT) on 2024 October 10 (PI E. Hammerstein). The spectrum was reduced using `PypeIt` (J. Prochaska et al. 2020; J. X. Prochaska et al. 2020) and standard optical spectroscopic reduction techniques, including bias subtraction, flat-fielding, flux calibration, coaddition, and telluric correction. Optical spectra are presented in Figure 2 and Table B4.

We present a total of four epochs of NIR spectroscopy of AT 2024wpp in Figure 3. These spectra are listed in Table B5, and we overview reduction details below.

Three epochs of *JH* and two epochs of *HK* NIR spectra of AT 2024wpp were obtained with the Flamingos-2 instrument (S. S. Eikenberry et al. 2004; S. Eikenberry et al. 2012) mounted on the Gemini-South Telescope (PI N. LeBaron). The additional *JH* spectrum was obtained owing to technical issues preventing the full *JH* + *HK* spectroscopy sequence from being obtained on 2024 October 16. The spectra were reduced with `PypeIt`, which performed flat-fielding, background subtraction, and source detection and extraction. The science

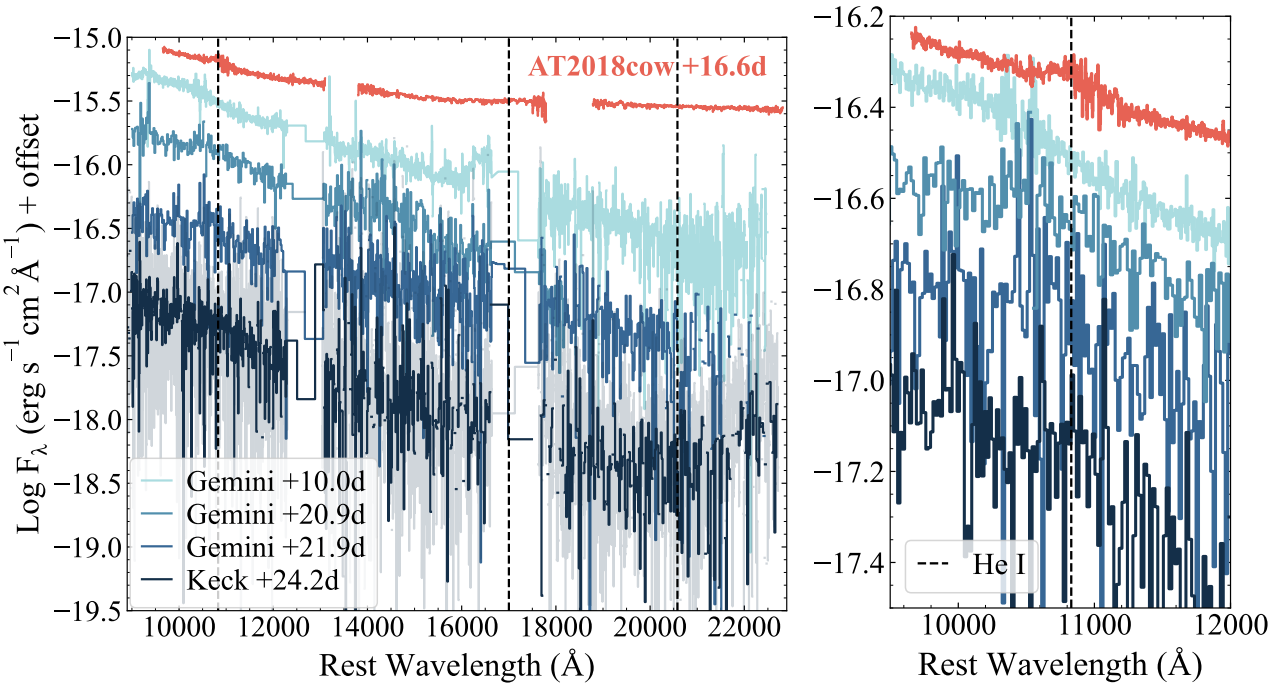

Figure 3. Left: AT 2024wpp NIR spectral series from +10.0 to +24.2 days after t_0. Spectra are plotted in the rest frame and are binned and scaled for clarity (for reference, the native binning is shown for the +24.2-day spectrum in lighter shading). For comparison, a +16.6-day spectrum of AT 2018cow (R. Margutti et al. 2019), the only other LFBOT with NIR spectra, is plotted. In contrast to the AT 2018cow spectrum, the AT 2024wpp spectra show no signs of He feature development by day 24. Right: zoom-in on the 1.08 μm He I feature.

spectra were then flux-calibrated, coadded, and corrected for telluric absorption, using the A0 V star HIP12858, which was observed directly after AT 2024wpp.

We also observed AT 2024wpp with the Near-InfraRed Echellette Spectrometer (J. C. Wilson et al. 2004; NIRES) on the Keck II 10 m telescope on 2024 October 20 as part of the Keck Infrared Transient Survey (S. Tinyanont et al. 2024). The observations were performed with two sets of the ABBA dithering pattern to sample the sky background, with a total exposure time of 2200 s. The A0 V star HIP14627 was observed immediately after the LFBOT to provide flux and telluric calibration. We reduced the data using `PypeIt` following the procedure outlined by S. Tinyanont et al. (2024).

3. Bolometric Luminosity and Inferred Properties

Similar to AT 2018cow, at $\delta t \leqslant 45$ days the UV-to-optical radiation from AT 2024wpp is dominated by a blackbody spectrum. The extremely blue colors and color evolution of AT 2024wpp impose nonnegligible deviations from the standard UVOT count-to-flux conversion factors. We account for this effect self-consistently in our blackbody fits by following the prescriptions by P. J. Brown et al. (2010)—that is, we iteratively recalibrate the fluxes with the input blackbody temperature until the input and output temperature agree to within uncertainties, as done for AT 2018cow (R. Margutti et al. 2019). We find that with a peak bolometric luminosity $L_{\rm pk} \approx 10^{45}$ erg s^{-1} and a rise time of $t_{\rm rise} \approx 4$ days (estimates in agreement with M. Pursiainen et al. 2025), AT 2024wpp is the most luminous known FBOT (Figure 4). Reaching an absolute UV magnitude of ~ -22.98, AT 2024wpp was $\sim$4.5 times more UV-luminous at peak than the prototypical event AT 2018cow.

We show the best-fitting blackbody parameters (temperature $T(t)$ and radius $R(t)$) in Figure 5. AT 2024wpp displays a high temperature ($T > 30{,}000$ K) in the first week of evolution and maintains $T \gtrsim 20{,}000$ K until the end of our monitoring, again in strict similarity with AT 2018cow but in stark contrast with SNe (see, e.g., L. Dessart et al. 2011). Our inferred temperatures are higher around peak than those presented by M. Pursiainen et al. (2025), which could be attributed to our iterative recalibration of the UV fluxes as described previously. Without this correction, we obtained similar temperatures to M. Pursiainen et al. (2025), and our fits settle at $T \gtrsim 20{,}000$ K, consistent with their analysis at epochs at which the recalibration is less impactful. We note that a "lack of cooling with time" is also a hallmark observational feature of TDEs (S. van Velzen et al. 2011). The initial blackbody radius of AT 2024wpp is $R \approx$ (1–2) $\times 10^{15}$ cm. This radius shows limited increase in the first few days before later decreasing monotonically with time, again in contrast with ordinary SNe, where the photospheric radius typically shows a linear increase with time during the first few weeks (L. Dessart et al. 2011). This evolution implies an initial average blackbody "expansion velocity" (defined as R/t) as high as $\sim$(0.2–0.3)c, decreasing to $<$6400 km s^{-1} at $\delta t \geqslant 20$ days. We note that the initial high expansion velocities are similar to those inferred from radio modeling of the blast wave in Paper II, by analogy to AT 2018cow. This, in addition to the more luminous AT 2024wpp having slightly higher velocities than AT 2018cow, points to a connection between LFBOT optical and radio emission components. We also note that blueshifted spectral features with $v \approx 6400$ km s^{-1} appear in the time period $\delta t = 16$–30 days (Figures 6-7), consistent with the idea that the recession of the blackbody radius inward revealed slower material in the LFBOT. The velocity and time of appearance of the spectral features associated with slowly moving material make it consistent with ejecta launched at t_0.

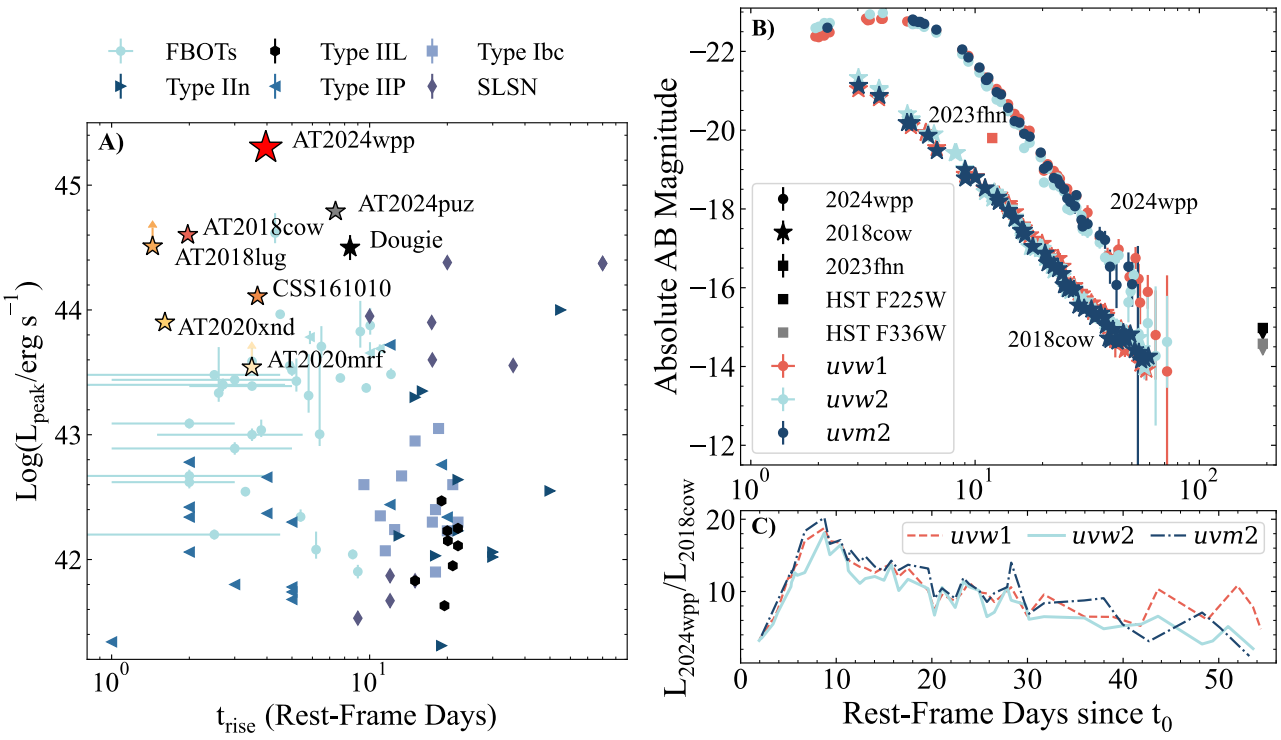

Figure 4. AT 2024wpp is the most luminous LFBOT discovered to date. (a) AT 2024wpp in the phase space of peak bolometric luminosity vs. rise time (rest frame) for FBOTs and other transients. Colored (grayscale) stars represent LFBOTs (likely LFBOTs). References: AT 2018cow (R. Margutti et al. 2019; D. A. Perley et al. 2019), CSS 161010 (C. P. Gutiérrez et al. 2024), AT 2018lug (A. Y. Q. Ho et al. 2020), AT 2020xnd (D. A. Perley et al. 2021), AT 2020mrf (Y. Yao et al. 2022), Dougie (J. Vinkó et al. 2015), AT 2024puz (J. J. Somalwar et al. 2025), FBOTs (M. R. Drout et al. 2014; I. Arcavi et al. 2016; M. Pursiainen et al. 2018), SNe Ibc (M. W. Richmond et al. 1996; P. A. Mazzali et al. 2000; F. Patat et al. 2001; M. Stritzinger et al. 2002; Y. Yoshii et al. 2003; P. Ferrero et al. 2006; P. A. Mazzali et al. 2006; S. Taubenberger et al. 2006; S. Valenti et al. 2008; D. J. Hunter et al. 2009; M. Modjaz et al. 2009; G. Pignata et al. 2011; S. Valenti et al. 2011), SLSNe (R. M. Quimby et al. 2011; C. Inserra et al. 2013), SNe IIP (M. Hamuy 2003), SNe IIn (M. Kiewe et al. 2012; R. Margutti et al. 2014), SNe IIL (I. Arcavi et al. 2012). We calculate peak pseudobolometric luminosities of LFBOTs AT 2018lug, AT2020xnd, and AT2020mrf using their peak g-band magnitudes (i.e., $L_{\rm pk} = \nu_g L_{{\rm pk},\nu_g}$). For FBOTs, SLSNe, and some SNe Ib/c, we similarly plot pseudobolometric luminosities. (b) Comparison of the three best-sampled LFBOTs in the UV (extinction-corrected, host-subtracted absolute magnitudes). For AT 2023fhn, we report the HST results from A. A. Chrimes et al. (2024a) for aperture photometry performed using a $0\farcs4$ annulus background and an extinction-corrected Swift $w1$ observation (see Appendix A for reduction details). Swift UVOT observations of AT 2024wpp captured the rise of an LFBOT and the evolution of an LFBOT at $\delta t \gtrsim 60$ d for the first time at UV wavelengths. (c) AT 2024wpp is ∼4.5 times more UV-luminous than the prototypical event AT 2018cow at peak, and it is the most UV-luminous FBOT discovered to date.

While the overall UV–NIR bolometric emission is well fit by a blackbody continuum, we find evidence for an excess of NIR emission at $\delta t = 30.0$ days but no evidence for an NIR excess from our broadband photometry at day 10.3. Section 6 discusses the observational properties of the NIR excess, its connections with a similar excess reported for AT 2018cow, and potential scenarios that can explain our observations.

We end with a few considerations. First, we derive an order-of-magnitude estimate of the ejecta mass $M_{\rm ej}$ at peak brightness, under the assumption that the rise time $t_{\rm rise}$ reflects the diffusion time of radiation from a centrally located source within ejecta expanding with typical velocity $v_{\rm ej}$. Following, for example, R. Margutti et al. (2019),

$$M_{\rm ej} \approx \frac{4\pi t_{\rm rise}^2 v_{\rm ej} c}{\kappa} \approx 2.0\, M_\odot \left(\frac{0.1\,{\rm cm^2\,g^{-1}}}{\kappa}\right)\left(\frac{v_{\rm ej}}{0.3c}\right)\left(\frac{t_{\rm rise}}{4\,{\rm days}}\right)^2, \quad (1)$$

where κ is an order-of-magnitude estimate of the opacity,[43] and we have adopted an ejecta velocity of $0.3c$ as indicated by our blackbody fits in Figure 5 (for $v_{\rm ej} = 0.2c$, $M_{\rm ej} \approx 1.4\,M_\odot$). The implied corresponding kinetic energy of the optically emitting material is large: $E_k \approx$ (5–15) $\times\ 10^{52}$ erg (compared to (0.03–0.3) $\times\ 10^{52}$ erg inferred for AT 2018cow; R. Margutti et al. 2019), effectively ruling out ordinary stellar explosions. The estimated $M_{\rm ej}$ for AT 2024wpp is larger than that inferred for AT 2018cow with the same approach (∼0.1–0.5 $M_\odot$ from R. Margutti et al. 2019), consistent with the longer rise time to peak but overall similar blackbody initial expansion velocity. We note that Equation (1) is an upper limit as $t_{\rm rise} = \max(t_{\rm diff}, t_{\rm visc})$ (see example in B. D. Metzger 2022a). Under other methods and assumptions (e.g., following N. Roth et al. 2016; T. Matsumoto & T. Piran 2021), we find $M_{\rm ej} \lesssim 1\,M_\odot$.

Post-peak, the UVOIR bolometric light curve decays as $L_{\rm UVOIR} \propto t^{-3.4}$, steeper than the evolution of AT 2018cow (R. Margutti et al. 2019; D. A. Perley et al. 2019), for which $L_{\rm UVOIR} \propto t^{-2.5}$ (Figure 8). Defining the "engine luminosity" as $L_{\rm engine} \equiv L_{\rm X} + L_{\rm UVOIR}$ (where $L_{\rm X}$ is the soft X-ray luminosity integrated in the range 0.3–10 keV; $L_{\rm engine}$ is a relevant quantity *if* the thermal UVOIR emission and the soft X-rays are a manifestation of the same physical component; see R. Margutti et al. 2019) and using the X-ray results from Paper II, we find a similar temporal evolution $L_{\rm engine} \propto t^{-3}$ at $\delta t \leqslant 100$ days, again steeper than in AT 2018cow, for which $L_{\rm engine} \propto t^{-2}$ in this time interval (R. Margutti et al. 2019, their Figure 9). However, by analogy with AT 2018cow, we

[43] The electron scattering opacity for fully ionized, H-depleted ejecta is $\kappa_{\rm es} \approx 0.2\ {\rm cm^{-2}\ g^{-1}}$.

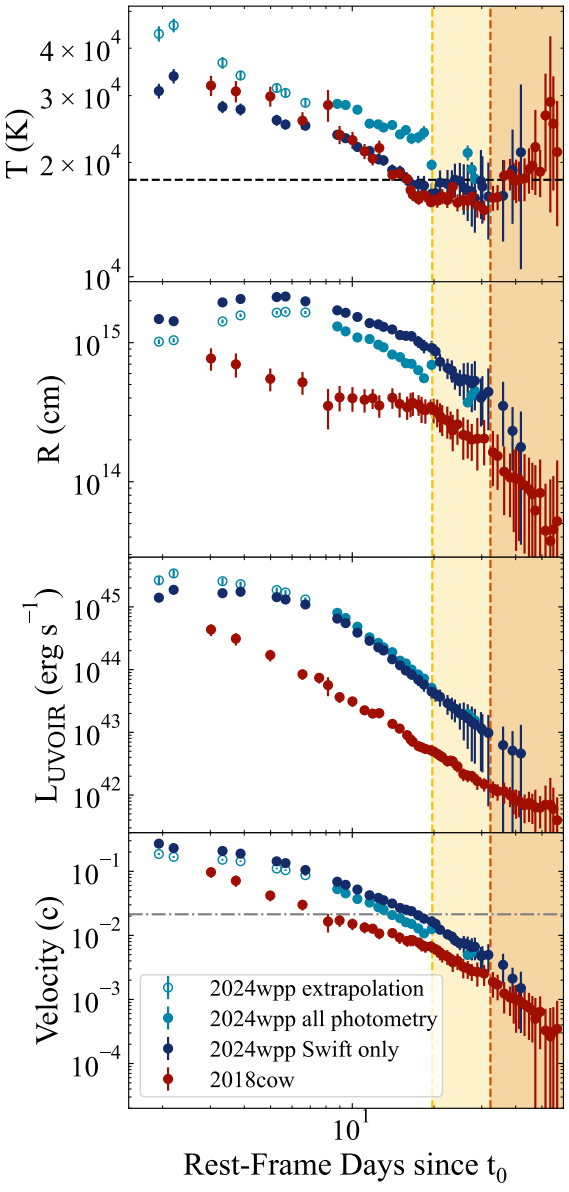

Figure 5. Temporal evolution of the best-fitting blackbody temperature T, radius R, bolometric luminosity $L_{\rm UVOIR}$, and blackbody expansion velocity of AT 2024wpp (shades of blue) compared to AT 2018cow (red) from R. Margutti et al. (2019). Dark (light) blue filled points: results from the Swift (Swift +LCO+Gemini) photometry. Open circles assume the color extrapolation presented in Figure 13 for $w1$—r and $w1$—i between days +2 and +7 from t_0. AT 2024wpp reaches $T > 30{,}000$ K (potentially as high as $\gtrsim$40, 000 K), and similarly to AT 2018cow, the T plateaus at late times around $T \approx 20{,}000$ K (horizontal dashed black line in the top panel). Yellow and orange shaded areas indicate the time of emergence of spectroscopic features in AT 2018cow and AT 2024wpp, respectively. The horizontal gray dashed–dotted line marks a velocity of $\sim$6400 km s^{-1}, which corresponds to the observed blueshift velocity of spectroscopic features that emerge between +16 and +30 days (see Figure 2).

find that optical spectroscopic features emerge in AT 2024wpp when $L_{\rm UVOIR} \approx L_{\rm X}$.

The total radiated energy by each emission component is listed in Table 1. From this table we note that during the first $\sim$45 days AT 2024wpp radiated $>10^{51}$ erg, a value that is only matched by the most luminous and long-lasting stellar explosions, such as superluminous SNe (SLSNe; R. M. Quimby et al. 2011), and that rules out ordinary SNe for which the *kinetic* energy is $\sim 10^{51}$ erg. As a comparison, AT 2018cow radiated $\sim 10^{50}$ erg during the first 60 days of evolution (R. Margutti et al. 2019, their Table 1).

Table 1
Energy Radiated by AT 2024wpp in the Time Interval $\delta t =$ 2–45 days

Component	Energy Radiated (erg)
Swift-only Blackbody[a]	$1.11^{+0.03}_{-0.03} \times 10^{51}$
Soft X-rays[b]	$2.8^{+0.1}_{-0.1} \times 10^{49}$
$E_{\rm engine}$[c]	$1.15^{+0.03}_{-0.03} \times 10^{51}$

Notes.
[a] Using blackbody parameters derived from only the Swift photometry (see Figure 5).
[b] 0.3–10 keV.
[c] Derived from $L_{\rm engine}$ in Figure 8.

4. A Persistent, Mostly Featureless, Optical-to-NIR Thermal Continuum

A distinct observational trait of LFBOTs is the combination of an almost completely featureless optical-to-NIR spectrum with a thermal continuum over a long timescale of weeks after first light. The prominently thermal continuum indicates an optically thick environment, and its persistence with time indicates that this environment is maintained over timescales of weeks. This combination can be obtained with either (i) a large ejecta mass or (ii) slowly expanding ejecta as we show below. For ejecta with mass $M_{\rm ej}$, maximum velocity $v_{\rm max}$, and opacity κ, in homologous expansion, the optical depth is

$$\tau \approx 160 \left(\frac{M_{\rm ej}}{2\,M_\odot}\right)\left(\frac{\kappa}{0.1\ {\rm cm^2\ g^{-1}}}\right)\left(\frac{v_{\rm max}}{0.3c}\right)^{-2}\left(\frac{t}{\rm days}\right)^{-2}, \quad (2)$$

where we have assumed a constant density profile in radius and a minimum ejecta velocity $\ll v_{\rm max}$. The optically thick condition ($\tau > 1$) up to $\delta t \approx 45$ days requires either fast-moving heavy ejecta with $M_{\rm ej} \gtrsim 26\,M_\odot$ and $v_{\rm max} \approx 0.3c$ or light ejecta with $M_{\rm ej} \approx 2\,M_\odot$ and $v_{\rm max} \leqslant 20{,}000$ km s^{-1}. A large ejecta mass would violate the constraints from the rapid rise time of AT 2024wpp, which indicates $M_{\rm ej} \lesssim 2\,M_\odot$,[44] while the low maximum expansion velocities are inconsistent with the inferred $R_{\rm phot}/t \geqslant 0.2c$ (Figure 5).[45] Another way to put this is that ejecta mass with $\lesssim 1\,M_\odot$ expanding at $v_{\rm max} > 20{,}000$ km s^{-1} would be optically thin by 45 days, producing optical spectra rich with well-defined spectral features (as in SNe) and thus violating our observations of AT 2024wpp. From another perspective, if $\tau(t_{\rm pk}) \approx v/c \approx$ 3–5 and $\tau(t) \propto t^{-2}$, then we would expect an optically thin spectrum after 1–2 weeks. A solution to this problem is the *continuous* deposition of ejecta mass similar to a wind (as opposed to one episode of ejection, like in an SN), which will keep the optical depth large even if matter is expanding fast and diluting, and/or multiple outflow components with different velocities dominating the detected emission at different epochs.

[44] We note that this is under the assumption that the rise time tracks the diffusion timescale from a centrally located energy source (as opposed to shock-heated material instead).
[45] In principle, the presence of *preexisting* material in the transient environment can alleviate this problem, but it would not naturally produce Doppler-broadened spectral features with $v \approx$ a fraction of c in the early-time ($\delta t \lesssim 10$ days) spectra.

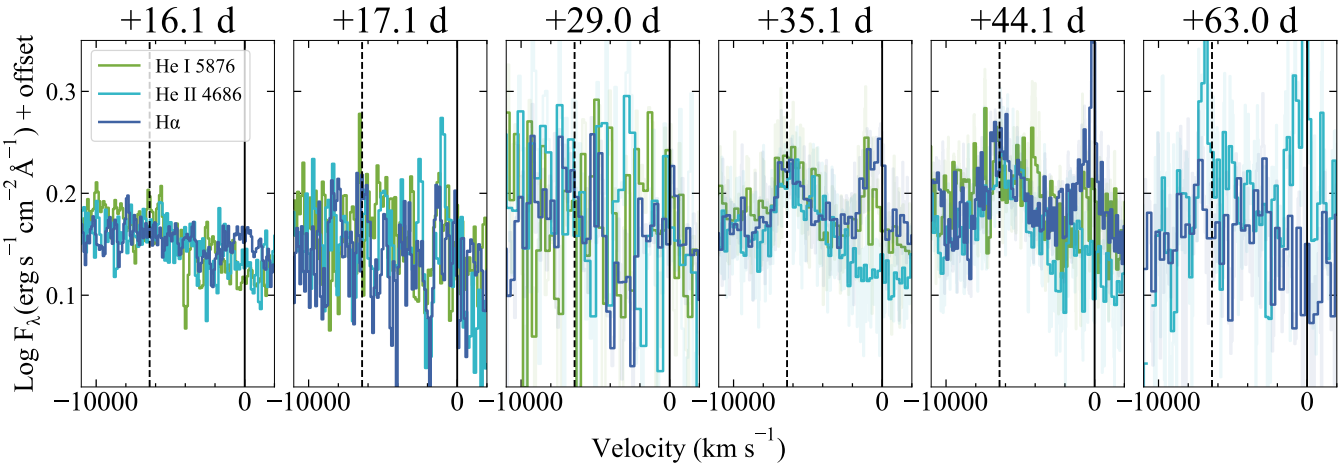

Figure 6. By +35 days, AT 2024wpp shows the emergence of clear Hα and He features blueshifted by $\sim$6400 km s^{-1}(dashed black line). The FWHM values of the blueshifted features stay consistently near $\sim$2000 km s^{-1} over the final three epochs. A blend of narrow host galaxy emission and a slightly broader spectral feature base from AT 2024wpp are also evident at 0 km s^{-1}, especially for Hα and He I. We do not identify a He I feature in the +63-day spectrum and thus omit that wavelength region for visual clarity. The lightly shaded spectra indicate native binning.

At the same time, the persistently featureless spectra can be the (combined) result of three main physical scenarios: (i) a steep ejecta density profile above the photosphere, which implies a very small line-forming region, such that the line flux would be negligible and very hard to detect against the bright, thermal continuum; (ii) extremely large expansion velocities ($\gtrsim$0.1c–0.3c) that lead to extreme Doppler broadening and line smearing; and (iii) extreme ionization of the ejecta such that recombination is prevented. Option (i) is the main factor leading to the blue and featureless spectra of SNe IIP at very early times. However, in the absence of a central energy source, scenario (i) would lead to the development of strong spectral lines as the ejecta expand and the photosphere recedes in mass coordinates (as observed in SNe), which are not observed in LFBOTs. Interestingly, high ionization has been invoked in the context of TDEs as a way to depress line formation (e.g., J. Guillochon et al. 2014; N. Roth et al. 2016 and references therein) and, given the observational similarities between TDEs and LFBOTs, might play a role in LBOTs as well.

In the following we thus consider a framework with the following key physical ingredients to explain the observed phenomenology: continuous energy deposition, a luminous central energy source that overionizes the ejecta, extreme Doppler broadening, and multiple outflow components. A similar model was proposed for AT 2018cow (R. Margutti et al. 2019), and we speculate on the astrophysical implications in Section 7. The viability of this model will be quantitatively explored in detail by O. Aspegren et al. (2025, in preparation) with non–local thermodynamic equilibrium numerical simulations with `Sedona` (D. Kasen et al. 2006). In this framework, by $t_{\rm pk}$, the "engine" has deposited $\leqslant 2\,M_\odot$ of ejecta and the optical/UV emission is a combination of reprocessing of X-rays from the central source and thermalization of the kinetic energy of the outflow (e.g., B. D. Metzger 2022a; D. Tsuna & W. Lu 2025).

5. The Emergence and Properties of Optical Spectral Features

5.1. Delayed Appearance of Spectral Features

Similar to AT 2018cow (R. Margutti et al. 2019; A. L. Piro & W. Lu 2020; D. Calderón et al. 2021; B. D. Metzger 2022a; P. Charalampopoulos et al. 2025), we hypothesize that around the optical peak brightness the UV–optical emission is dominated by partial reprocessing of the highly variable, inner X-ray source by fast polar outflows (i.e., the *external* shock interaction is subdominant, as supported by the coupled evolution, similar luminosities at late times, and highly variable nonthermal X-ray emission). In this scenario, the temporal evolution of $L_{\rm X}/L_{\rm UVOIR}$ in Figure 9 directly depends on the reprocessing efficiency of the outflow, and hence on its density, temperature, and ionization state (with lower-density, higher-ionization material having a lower reprocessing efficiency). Figure 9 shows that $L_{\rm X}/L_{\rm UVOIR}$ increases from $\sim$0.01 at optical peak to $\lesssim$1 at the time of emergence of clear spectral features with a width of a few $\times$ 10^3 km s^{-1} at $\delta t \approx 30$ days. Interestingly, a similar pattern is followed by AT 2018cow; however, AT 2018cow has consistently larger $L_{\rm X}/L_{\rm UVOIR}$ values and reaches $L_{\rm X}/L_{\rm UVOIR} \approx 1$ at an earlier stage (with related earlier appearance of the spectral features). This phenomenology is consistent with the observed longer rise time and larger mass of the polar outflow that we inferred for AT 2024wpp (Section 4) compared to AT 2018cow.

An increasing ratio $L_{\rm X}/L_{\rm UVOIR}$ with time is expected as a result of (i) the expansion of the polar outflow, which leads to lower densities, and/or (ii) increasing ionization of the ejecta (B. D. Metzger et al. 2014; D. Tsuna & W. Lu 2025). Both factors are likely at play and lead to a decrease of the effective opacity with time (as shown in Figure 10), thus allowing inner regions to be revealed, while at the same time reducing the effects of line smearing due to photon scattering. The latter effect creates line profiles with broad scattering wings and might make the emission lines effectively undetectable against the continuum at times of larger optical depths, as proposed by D. Tsuna & W. Lu (2025). The blackbody radius evolution paints a similar picture. At early times ($\delta t < 6$ days) we find evidence for an expanding blackbody radius[46] (Figure 5), indicating a brief period of time during which the polar outflow can carry out the photosphere with an inferred velocity of 0.2c–0.3c. This brief phase is absent in the observations of AT 2018cow, again consistent with the smaller mass of the

[46] We note that in similarity to SNe II (e.g., I. Rabinak & E. Waxman 2011), the blackbody-inferred radius is a better proxy for the photon thermalization radius instead of the photospheric radius where $\tau_{\rm es} \approx 1$.

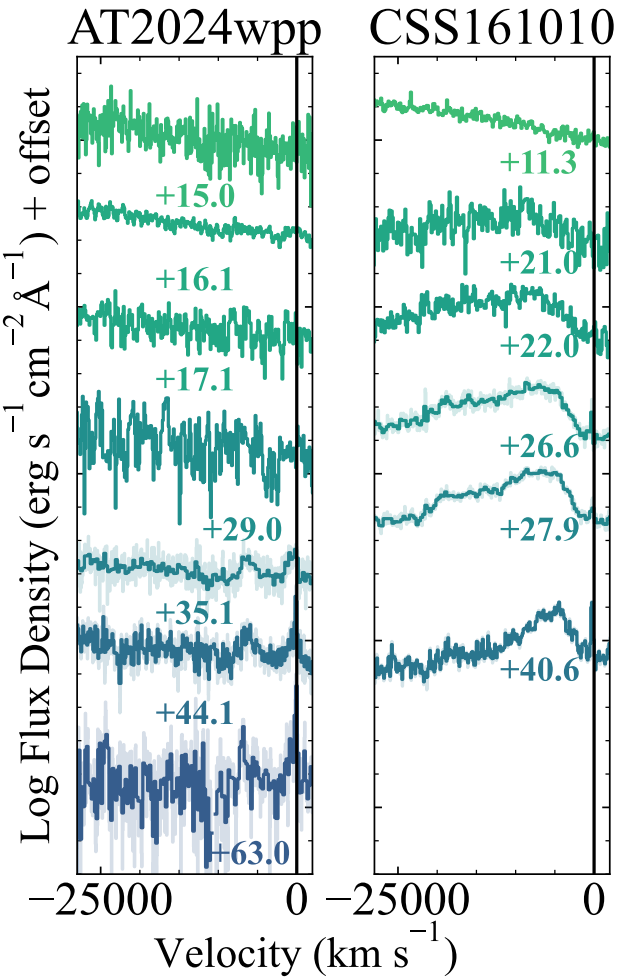

Figure 7. Evolution of the Hα line in AT 2024wpp (left) and CSS161010 (right; C. P. Gutiérrez et al. 2024), the two LFBOTs with evidence for blueshifted emission. The $v = 0$ km s^{-1} component in CSS161010's spectrum is narrow host galaxy emission. In AT 2024wpp, the component is broader (FWHM $\approx$ 2000 km s^{-1}, similar to the blueshifted component; see Figure 11); thus, we identify it as a transient emission feature. The lightly shaded spectra indicate native binning.

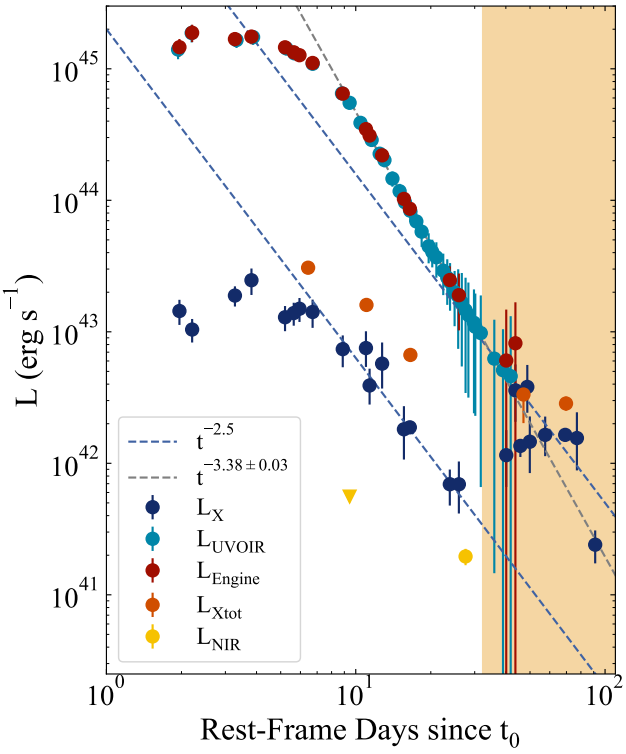

Figure 8. Soft X-ray (0.3–10 keV; L_X, dark-blue circles), broadband X-ray (0.3–30 keV; L_{Xtot}, orange circles), NIR (fitted power-law luminosity in the range 2000–24,000 Å; L_{NIR}, yellow circles), and UVOIR bolometric luminosity (L_{UVOIR}; teal circles) evolution of AT 2024wpp in its first 100 days. We also show the "engine luminosity" $L_{engine} \equiv L_X + L_{UVOIR}$ with dark-red circles. We find that at 10 days $< \delta t <$ 30 days, $L_{engine} \propto t^{-3.4}$ (gray dashed line) and that a similar scaling applies to L_{UVOIR} at 10 days $< \delta t <$ 30 days, while $L_X \propto t^{-2.5}$ (blue dashed line). At $\delta t >$ 30 days, there is some indication that the decay of L_{engine} flattens slightly toward the $t^{-2.5}$ power law. The orange shaded area marks the time of appearance of clear spectral features ($\delta t \approx$ 16–30 days; Figures 2 and 6). X-ray data from Paper II.

polar outflow in this event. At $\delta t \gtrsim 6$ days, the inferred radius of the blackbody that best fits the UV–optical emission monotonically decreases with time. The recession of the optical photosphere allows slower-moving ejecta components to be revealed and line emission to emerge. In line with this argument, at the time of emergence of spectral features, the H+He line-forming region of AT 2024wpp is roughly at a radius $R_{line} \approx 6500\,\mathrm{km\,s^{-1}} \times \delta t \approx 2 \times 10^{15}$ cm $> R_{BB,\,30d}$, under the assumption that the slower-moving ejecta was launched at t_0. We conclude that the line emission in AT 2024wpp is consistent with originating from an inner region of the ejecta with lower expansion velocities ($\sim$6500 km s^{-1} vs. 0.2c–0.3c) that is revealed only at later times because of optical-depth-related effects (e.g., Figure 10).

Interestingly, we do not observe a continuum of outflow velocities; rather, in addition to the mildly relativistic outflows with $\sim$0.2c–0.3c, our spectra indicate only two components centered at 6500 and 0 km s^{-1} with similar values of the full width at half-maximum (FWHM) intensity, $\approx$few $\times$ 10^3 km s^{-1}. This peculiar dual-component profile where the FWHM is less than the blueshift of the centroid is observed for both the H and He features. Thus, the line-forming regions of both elements (which are likely distinct; see, e.g., N. Roth et al. 2016) share similar physical conditions and kinematics. Line formation in an outflowing medium that is dominated by electron scattering has been demonstrated to lead to blueshifted line profiles (e.g., see models for TDEs such as N. Roth & D. Kasen 2018). However, for a homologously expanding outflow, this model leads to a blueshifted component with a profile width that is commensurate with the displacement of the line centroid, together with a prominent red wing (e.g., Figure 6 of N. Roth & D. Kasen 2018), which contrasts with our observations of AT 2024wpp. We thus consider it likely that the line profiles of Figures 6–7 indicate a deviation from spherical symmetry of the emitting region.[47] This is not necessarily inconsistent with the low polarization of AT 2024wpp measured between 6 and 14 days (M. Pursiainen et al. 2025), as the weak spectral features indicating asphericity do not appear until at least $\sim$20 days. Thus, AT 2024wpp may be more spherical at early times before the photosphere recedes and the inner ejecta structure is revealed. Similar to AT 2018cow, these observations are consistent with a model where the H+He emission originates from lower-velocity equatorial material, with polar outflows

[47] There are known nonpurely kinematic effects that can lead to blueshifted line profiles even in bulk-receding ejecta (B. F. A. van Baal et al. 2023). However, it is not clear whether these physical conditions apply here, and we leave to future work the detailed exploration of this aspect.

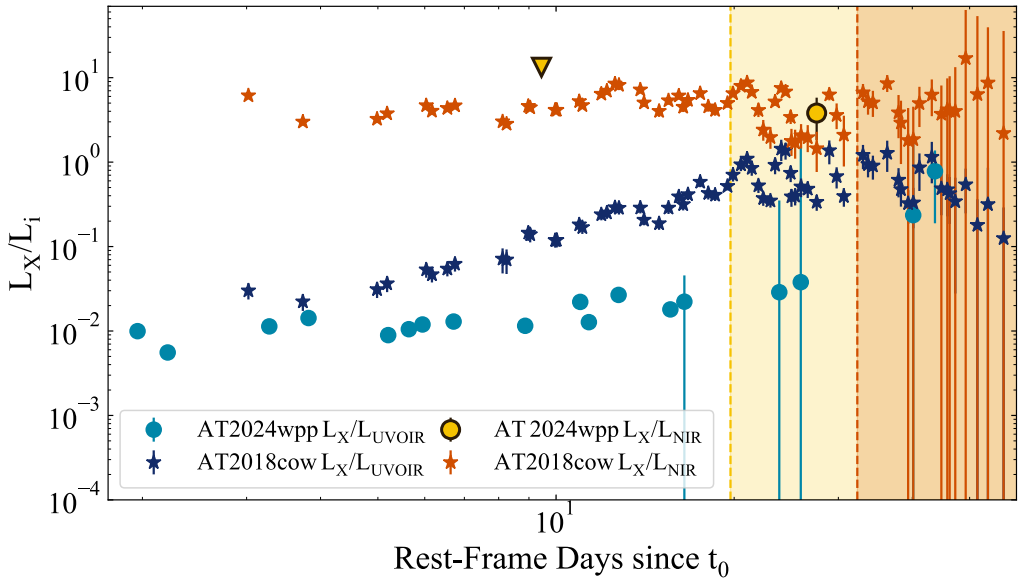

Figure 9. Ratio of the soft (0.3–10 keV) X-ray luminosity (L_X) to L_{UVOIR} (shades of orange) and L_{NIR} (shades of blue; see Section 6) for AT 2024wpp (circles) and AT 2018cow (stars). L_{UVOIR} is calculated from the blackbody fits (see Figure 5). The shaded yellow (orange) area marks the time of emergence of clear spectral features with widths of a few $\times$ 10^3 km s^{-1} in AT 2018cow (AT 2024wpp). Interestingly, for both events this happens for $L_X \approx L_{UVOIR}$. This plot also shows that $L_X/L_{NIR} \approx$ constant with time for AT 2018cow and that the parameters of AT 2024wpp are consistent with the same value. AT 2018cow data from R. Margutti et al. (2019); AT 2024wpp L_X data from Paper II.

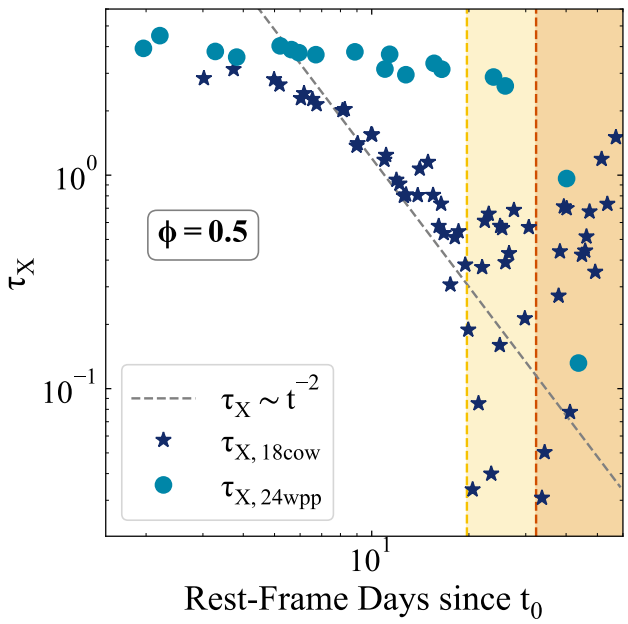

Figure 10. Assuming that the observed L_{UVOIR} is purely due to radiative processing of X-rays (B. D. Metzger 2022a) occurring within (an arbitrary) 50% of the solid angle (parameterized by ϕ; in the other half, we assume that all X-rays are reprocessed), we calculate the associated τ_X for AT 2024wpp (circles) and AT 2018cow (stars) over time and compare to the time of emergence of spectral features (vertical dashed lines; same as Figure 9) for each object. The gray dashed line represents the canonical scaling ($\tau_X \propto t^{-2}$) for radiation escaping a medium expanding at constant velocity. We find that AT 2024wpp maintains a higher τ_X for longer compared to AT 2018cow. This is consistent with the features of AT 2024wpp emerging at a later epoch and with the larger inferred M_{ej} (Section 3).

carrying the mildly relativistic ejecta (R. Margutti et al. 2019, their Figure 12; Paper II, their Figure 14). These conditions are naturally realized in super-Eddington accretion disks (e.g., A. Sadowski & R. Narayan 2015; A. Sądowski & R. Narayan 2016). Interestingly, radiation-hydrodynamic simulations of super-Eddington accretion flows around BHs by S. Yoshioka et al. (2024) found evidence for two components of outflows, with a faster, lighter component having velocity $\gtrsim 0.1c$ ejected along the polar direction (i.e., within $\sim 10°$) and slower, denser outflows having typical velocities of a few $\times$ 10^3 km s^{-1} at larger angles (their Figure 4). The presence and properties of these two outflow components are consistent with the observations of AT 2024wpp and LFBOTs that have detailed spectroscopic sequences.

In Figure 11, we compare the evolution of the FWHM, velocity offset from line center, and EW of AT 2024wpp's spectral features to other transients. To date, CSS161010 is the only other FBOT to show blueshifted spectral features; these features are up to a factor of 10 broader than those observed in AT 2024wpp and are blueshifted by $\sim$10,000 km s^{-1}, other than the final epoch at 40 days, which is blueshifted by $\sim$6500 km s^{-1}, similar to AT 2024wpp's features. Neither AT 2024wpp's nor CSS161010's line profiles show the red wing expected for an electron-scattering-dominated outflowing medium (N. Roth & D. Kasen 2018). A few TDEs show blueshifted spectral features: AT 2020wey possibly has blueshifted secondary Hα peaks in several optical spectra (P. Charalampopoulos et al. 2023), though the spectra have low S/N; PTF09ge (I. Arcavi et al. 2014), ASASSN-15oi (T. W. S. Holoien et al. 2016), and SDSS J0748 (T.-G. Wang et al. 2011) all exhibit blueshifted He II λ4686 in at least one epoch; and ASASSN-14ae (T. W. S. Holoien et al. 2014) and AT 2022dbl (X. Guo et al. 2025, in preparation) both show a blueshift of Hα in their earliest spectrum. Many of these TDE features can be at least partly explained by electron scattering (N. Roth & D. Kasen 2018), potentially alongside Bowen fluorescence feature blends for the He II profiles (see S. Gezari et al. 2015; J. S. Brown et al. 2018). We also note that TDE features tend to have much larger EWs than those measured for AT 2024wpp.

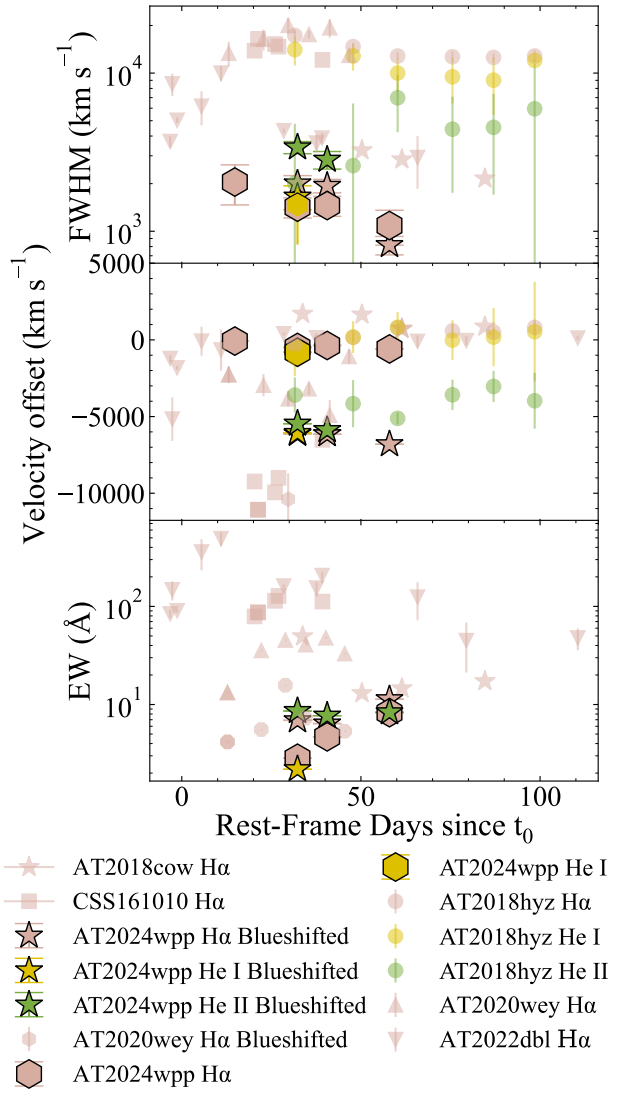

Figure 11. Evolution of the FWHM (top panel), velocity offset (middle panel; i.e., blueshift or redshift of line peak from the rest wavelength), and line EW (bottom panel) for the Hα (pink), He i λ5876 (gold), and He ii λ4686 (green) emission lines and associated blueshifted components of AT 2024wpp (outlined stars). AT 2024wpp exhibits unique spectral feature evolution compared to LFBOTs AT 2018cow (unoutlined stars) and CSS161010 (squares), as well as to TDEs AT 2020wey (upward-pointing triangles denote the spectral feature near the rest wavelength, and hexagons denote blueshifted components attributed to Hα by P. Charalampopoulos et al. 2023), AT 2018hyz (circles; P. Short et al. 2020), and AT 2022dbl (downward-pointing triangles; X. Guo et al. 2025, in preparation). Especially note the slight blueshift in time of the spectral features of AT 2024wpp.

5.2. Line Luminosity

Another peculiarity of the spectral features of AT 2024wpp is their low line luminosity and EW. Peaking at $L_{\rm H\alpha} \approx 10^{39}\,{\rm erg\,s^{-1}}$, the observed line luminosity is $\sim$0.01% of the bolometric luminosity at the same time. We follow the reasoning by D. Tsuna & W. Lu (2025, their Section 4.2) and consider a photoionization origin for the detected lines. For comparison, shock ionization of $1\,M_\odot$ of material would contribute at most $\sim 4 \times 10^{45}$ erg in Hα line assuming 100% efficiency, and we observed $\gtrsim 10^{45}$ erg. We thus consider shock ionization less likely. The amount of ionized mass ($M_{\rm ion}$) in the slow-moving ejecta can be either the total mass (density-bounded regime) or lower (ionization-bounded regime; e.g., D. E. Osterbrock & G. J. Ferland 2006).

In the ionization-bounded regime, the Hα line luminosity is (D. Tsuna & W. Lu 2025, their Equation (50))

$$L_{\rm H\alpha} \approx \dot{N}_{\rm ion}\,\epsilon_{\rm H\alpha}\left(\frac{\alpha_B^{\rm H\alpha}}{\alpha_B}\right), \tag{3}$$

where $\dot{N}_{\rm ion} \approx \Phi L_{\rm ion}/\epsilon_{\rm ion}$ is the photoionization rate; $L_{\rm ion}$ is the ionizing luminosity; Φ is the fraction of ionizing luminosity intercepted by the slow ejecta; $\epsilon_{\rm ion}$ is the energy "cost" for each hydrogen ionization, which depends on the details of photoionization and recombination of each species in the ejecta (here we use $\epsilon_{\rm ion} \approx 30\,{\rm eV}$ following D. Tsuna & W. Lu 2025); α_B is the recombination coefficient and $\alpha_B^{\rm H\alpha}$ is the Hα recombination coefficient; and $\epsilon_{\rm H_\alpha}$ is the Hα photon energy. For a typical recombination branching fraction of $\alpha_B^{\rm H\alpha}/\alpha_B \approx 1/3$, Equation (3) leads to the following Hα production efficiency:

$$\frac{L_{\rm H\alpha}}{L_{\rm ion}} \approx 10^{-2}\left(\frac{\Phi}{0.5}\right)\left(\frac{\epsilon_{\rm ion}}{30\,{\rm eV}}\right)^{-1}. \tag{4}$$

The significantly lower ratio observed, $L_{\rm H\alpha}/L_{\rm engine} \gtrsim 10^{-4}$, may be due to a significantly lower Φ (i.e., geometric effects), a small fraction of $L_{\rm engine}$ being ionizing photons, a H-depleted slow outflow (e.g., a tidally disrupted W-R star), or the fact that this is instead in the density-bounded regime.

The maximum ionized mass is given by Equation (49) from D. Tsuna & W. Lu (2025),

$$\begin{aligned} M_{\rm ion,max} &\approx m_p\sqrt{\frac{4\pi R_{\rm line}^3\,\Phi L_{\rm rad}/\epsilon_{\rm ion}}{3\alpha_B}} \\ &\approx 0.2\,M_\odot\left(\frac{\Phi}{0.5}\right)^{1/2} \\ &\quad\left(\frac{L_{\rm rad}}{10^{43}\,{\rm erg\,s^{-1}}}\right)^{1/2}\left(\frac{\epsilon_{\rm ion}}{30\,{\rm eV}}\right)^{-1/2} \\ &\quad\times\left(\frac{R_{\rm line}}{2\times10^{15}\,{\rm cm}}\right)^{3/2}\left(\frac{T}{10^5\,{\rm K}}\right)^{0.35}, \end{aligned} \tag{5}$$

where we used a fiducial value of $R_{\rm line} \approx 6000\,{\rm km\,s^{-1}} \times \delta t \approx 2\times10^{15}$cm for the radius relevant to the slower ejecta of AT 2024wpp.

If the actual mass of the ionized Hα-emitting gas, $M_{\rm ion}$, is much lower than $M_{\rm ion,max}$, we would be in the density-bounded regime, and hence the line production efficiency $L_{\rm H\alpha}/L_{\rm rad}$ will be lower than that in the ionization-bounded regime ($\sim$1%) by a factor of $M_{\rm ion}/M_{\rm ion,max}$. In the super-Eddington disk outflow picture, the majority of the mass is carried by the slowest outflow that originates from the outer disk. For an outer disk radius of R_d and compact-object mass M, we expect the velocity of the slowest outflow to be $v_{\rm min} \sim \sqrt{GM/R_d}$. The outflow near $v_{\rm H\alpha} \approx 6000\,{\rm km\,s^{-1}}$ is launched from smaller radii near $(v_{\rm min}/v_{\rm H\alpha})^2 R_d$, and hence the outflow mass near velocity $v_{\rm H\alpha}$ is roughly given by $M_{v_{\rm H\alpha}} \sim (v_{\rm min}/v_{\rm H\alpha})^{2p} M_d$, where M_d is the total disk mass and we have adopted a radial power-law scaling for the accretion rate in a super-Eddington disk $\dot{M}(r) \propto r^p$. For $p = 0.5$ (as adopted by D. Tsuna & W. Lu 2025), we expect

$$M_{v_{\rm H\alpha}} \sim 0.03\,M_\odot\frac{(M_d/M_\odot)(M/1.4\,M_\odot)^{1/2}}{(R_d/10\,R_\odot)^{1/2}}, \tag{6}$$

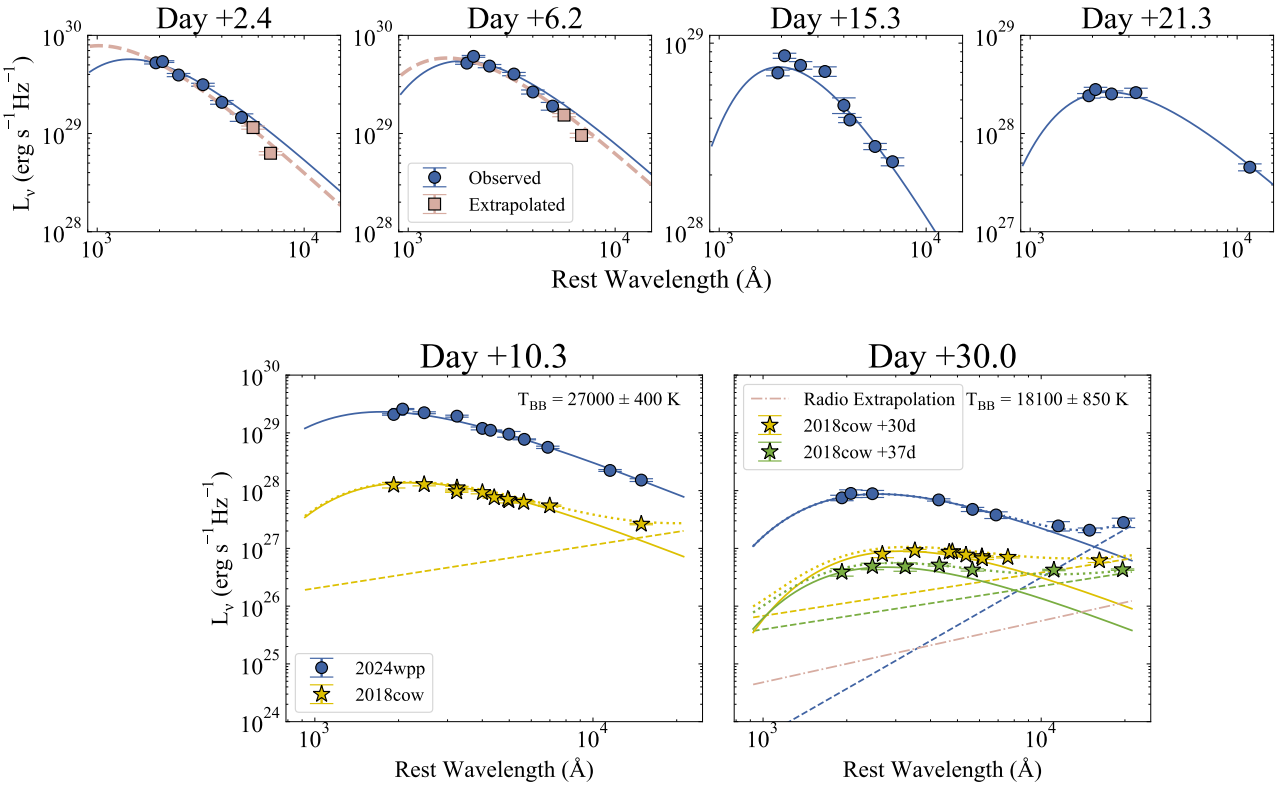

Figure 12. Top panel: blackbody fits to the observed photometry (blue points) at various epochs (observed-frame days). Pink points are extrapolated *r*- and *i*-band photometries that assume the *w*1–*r* and *w*1–*i* colors shown in Figure 13. Bottom panel: AT 2024wpp SEDs on the (observed-frame) days of its *J*- and *H*-band photometry compared to coeval SEDs of AT 2018cow. We find no evidence of emission in excess of a blackbody fit (blue curves) until day +30, at which time a blackbody plus power-law model (blue dashed curve) is required to fit the SED. The best-fit power law (blue dashed line; $F_\nu \propto \nu^{-\alpha}$) has $\alpha = 2.7 \pm 0.5$. AT 2024wpp is not fit well by the power law ($\alpha = 0.75$; yellow and green dashed lines) that D. A. Perley et al. (2019) and Y. Chen et al. (2023a) used to fit the NIR excess of AT 2018cow. Additionally, the extrapolation of the coeval radio SED (pink curve; from Paper II) cannot explain the observed NIR excess.

where we have adopted fiducial values of $M_d \sim M_\odot$ and outer radius $R_d \sim 10\,R_\odot$ as the disk loses mass and viscously spreads over time (assuming that the line emission comes from the freshly launched slow outflow). We find that the system may indeed be in the density-bounded regime, but this only reduces the line production efficiency by an order of magnitude to about 0.1% if $\Phi \approx 0.5$. Geometric effects ($\Phi \ll 1$) or a hydrogen-poor outflow may further reduce the line production efficiency to the observed value.

To conclude and summarize, the structure of the spectral features of AT 2024wpp points to an ejecta geometry with clear deviation from spherical symmetry involving multiple outflows including a fast, collimated component and a slower component. Outflows from disks accreting at super-Eddington rates are a plausible formation scenario of the observed dual-line-profile structure (see, e.g., S. Yoshioka et al. 2024).

6. An NIR Excess of Emission

The appearance of an NIR excess of emission at early times is a hallmark observational feature of LFBOTs.[48] We first summarize the key observational facts and then consider two interpretations: reprocessed radiation from a preexisting dust shell (i.e., a dust echo in Section 6.1), and frequency-dependent opacity effects due to free–free processes in the transient's outflows or preexisting material (Section 6.2).

The NIR observational results are as follows:

1. We find evidence for a deviation from the blackbody that best fits the UV–optical SED at NIR wavelengths. At $\delta t = 30.0$ days, the local power-law slope measured from our photometry in the NIR is $F_{\nu,\mathrm{NIR}} \propto \nu^{-\alpha}$ with $\alpha \approx 0.3$. Following D. A. Perley et al. (2019) and Y. Chen et al. (2023a), we fit the overall spectrum with a phenomenological model consisting of a blackbody + power law ($F_{\nu,\mathrm{BB}} + F_{\nu,\mathrm{PL}}$), finding $F_{\nu,\mathrm{PL}} \propto \nu^{-3}$ (Figure 12).
2. The NIR luminosity of AT 2024wpp at (rest frame) +27.6 days determined from $F_{\nu,\mathrm{PL}}$ (integrated in the range 2300 Å–2.4 μm) is $L_{\mathrm{NIR}} = (1.9 \pm 0.3) \times 10^{41}$ erg s^{-1}, which is comparable to the power-law luminosity of AT 2018cow at (rest frame) +29.8 days ($L_{\mathrm{NIR}}^{\mathrm{18cow}} = 3.0 \pm 0.6 \times 10^{41}$ erg s^{-1} over the same wavelength region, using the power-law parameters from Y. Chen et al. 2023a).
3. The NIR "excess" is clearly detected at $\delta t = 30.0$ days, but it was not detected in our previous epoch with NIR sampling at day +10.3, or in the final *z*-band epoch (day +17.9). Our Keck NIR spectroscopy at 24.2 days indicates $F_{\nu,\mathrm{NIR}} \propto \nu^{-\alpha}$ with $\alpha > 0$ (especially at wavelengths >1.9 μm; see Figure 3), consistent with the day +30 findings, suggesting that the NIR excess was already emerging at $\delta t = 20$ days (this aligns with the 20-day NIR excess reported by M. Pursiainen et al. 2025). At $\delta t = 10.3$ days we do not

[48] However, we note that similar NIR excesses have also been observed in SNe that are shrouded in very dense surrounding media (e.g., SN 2009ip; R. Margutti et al. 2014, their Figure 27; N. Smith et al. 2013, their Figure 2).

find significant evidence for a departure from a blackbody spectrum in the NIR, and we estimate a 3σ limit on the (undetected) NIR excess of $L_{\rm NIR} < 5.6 \times 10^{41}$ erg s^{-1}. We note that the later detection of an NIR excess in AT 2024wpp (20–30 days) compared with AT 2018cow, which showed an NIR excess within a few days, can be related to the significantly larger UV–optical luminosity of AT 2024wpp.

4. The ratio of the soft X-ray luminosity (0.3–10 keV) to the NIR power-law luminosity ($L_{\rm x}/L_{\rm NIR}$) for AT 2024wpp is consistent with that of AT 2018cow, remaining constant with time at $\sim$0.5 (Figure 9).
5. As in AT 2018cow (R. Margutti et al. 2019), the extrapolation of the radio spectrum of AT 2024wpp (from Paper II) to the NIR range significantly underpredicts the NIR flux (Figure 12), even in the absence of any spectral break in between the two wavelength regimes, implying that the NIR excess is not directly connected with the nonthermal radio synchrotron spectrum.

6.1. Dust Echo

Following B. D. Metzger & D. A. Perley (2023) and S. Tuna et al. (2025), we investigate whether the NIR excess can be explained by reprocessing of early UV emission by a preexisting, opaque, dusty medium. B. D. Metzger & D. A. Perley (2023) postulate that LFBOT progenitors may be surrounded by a dense and cool CSM at large radii ($\gtrsim 10^{16}$ cm) where dust can form before the LFBOT. This "dusty outer shell" would initially be opaque to UV photons until reaching sublimation temperatures ($\sim$2000 K). In this model the absorbed energy is reradiated as an NIR "echo" on a timescale mostly set by geometric time delays. The persistent NIR excess of AT 2018cow, observed during $\delta t = 3$–44 days, was interpreted by B. D. Metzger & D. A. Perley (2023) as a dust echo originating from a medium with density $n(r) = n_0 (r/r_0)^{-3}$ and $n_0 \approx 3 \times 10^7\,{\rm cm}^{-3}$ at $r_0 = 10^{16}\,{\rm cm}$ (assuming 1 μm silicate grains and a dust-to-gas ratio $X_d = 0.1$). We note that the assumed $n(r)$ scaling was motivated by the findings from the radio modeling. This model is appealing, as the derived medium density is not too different from that inferred from the radio modeling of AT 2018cow if large deviations from equipartition are considered (R. Margutti et al. 2019).

A similarly steep and dense CSM density profile is obtained from the radio modeling of AT 2024wpp (Paper II, their Figure 10), motivating us to explore the dust echo model for AT 2024wpp. Under the same model assumptions, the maximum duration of an NIR excess of emission is (B. D. Metzger & D. A. Perley 2023, their Equation (22))

$$\Delta t_{\rm IR,\,max} \approx 31.6\ {\rm days} \times \left(\frac{n_0}{10^7\,{\rm cm}^{-3}}\right)^{1/2} \left(\frac{r}{10^{16}\,{\rm cm}^3}\right)^{-3} \left(\frac{X_d}{0.1}\right) \left(\frac{a}{1\,\mu{\rm m}}\right)^{-1/2}. \quad (7)$$

The NIR excess in AT 2024wpp lasts $\geqslant$30 days and thus implies $n_0 \gtrsim 10^7\,{\rm cm}^{-3}$, similar to AT 2018cow. As a comparison, the CSM density inferred from the radio modeling of AT 2024wpp in equipartition is $n \approx 1 \times 10^5\,{\rm cm}^{-3}$ at 10^{16} cm (see Paper II). Similar to above, this density can only be comparable to the density of the NIR-emitting material derived above *if* corrections from a large deviation from equipartition are applied.

The predicted NIR luminosity (Equation (23) of B. D. Metzger & D. A. Perley 2023, here renormalized using the peak bolometric luminosity $L_{\rm pk}$ and rise time $t_{\rm pk}$ of AT 2024wpp) is

$$L_{\rm IR} \approx 3.2 \times 10^{40}\,{\rm erg\ \ s^{-1}} \times \left(\frac{n_0}{10^7\,{\rm cm}^{-3}}\right)\left(\frac{r}{10^{16}\,{\rm cm}^3}\right)^{-3} \left(\frac{X_d}{0.1}\right)\left(\frac{a}{1\,\mu{\rm m}}\right)^{1/2} \times \left(\frac{L_{\rm pk}}{2 \times 10^{45}\,{\rm erg\,s^{-1}}}\right)^{-1/2}\left(\frac{t_{\rm pk}}{4\ {\rm days}}\right). \quad (8)$$

The observed $L_{\rm NIR} = (1.9 \pm 0.3) \times 10^{41}$ erg s^{-1} thus implies $n_0 \approx 4 \times 10^7\,{\rm cm}^{-3}$, again consistent with the radio-inferred CSM density for large deviations from equipartition. In this scenario, while the NIR and the radio do *not* belong to the same component of emission, they can nevertheless originate from the same medium.[49]

6.2. Free–Free Opacity Effects in an Extended "Atmosphere"

P. Charalampopoulos et al. (2025) propose that an LFBOT NIR excesses can be related to free–free opacity effects occurring within an extended medium having a shallow density profile above the *optical* photosphere $r_{\rm ph}$. In this region at $r > r_{\rm ph}$, the absorptive opacity κ_a changes systematically with frequency—that is, different frequencies of the continuum spectrum will have different effective thermalization radii, producing a deviation from a single-temperature blackbody spectrum. This is analogous to the process that produces NIR/radio excesses in hot stars surrounded by dense winds (e.g., A. E. Wright & M. J. Barlow 1975; P. A. Crowther 2007), and it has been suggested by N. Roth et al. (2016) to play a major role in shaping the continuum in TDEs. Here we follow N. Roth et al. (2016), W. Lu & C. Bonnerot (2020), P. Charalampopoulos et al. (2025), and J. J. Somalwar et al. (2025) and assume that free–free dominates the absorptive opacity ($\kappa_a \approx \kappa_{\rm ff}$) and that in the extended atmosphere $\kappa_{\rm ff} \ll \kappa_{\rm es}$ (where $\kappa_{\rm es}$ is the electron scattering opacity), such that the effective opacity is $\kappa_{\rm eff} \approx (\kappa_{\rm ff}\kappa_{\rm es})^{1/2}$ (see G. B. Rybicki & A. P. Lightman 1979, chap. 1). In this treatment the medium is assumed to be effectively optically thick. We generalize the W. Lu & C. Bonnerot (2020) analytical model for a power-law density profile of the emitting medium above the optical photosphere $r_{\rm ph}$ of the form $\rho(r) = \rho_0 (r_0/r)^{-s}$. The specific luminosity is $L_\nu \approx 4\pi j_\nu V$, where j_ν is the emissivity; the emitting volume is $V = f r_{{\rm th},\nu}^3$ for a frequency-dependent thermalization radius $r_{{\rm th},\nu}$,

$$r_{{\rm th},\nu} = (0.018\kappa_{\rm es})^{\frac{1}{3s-2}} \left(\frac{\rho_0^{3/2} r_0^{3s/2} Z}{m_p \mu_e \mu_I^{1/2}(s-1)} T^{-3/4} \nu^{-1}\right)^{\frac{2}{3s-2}}, \quad (9)$$

where T is the temperature of the medium, m_p is the proton mass, Z is the atomic number, and μ_e (μ_I) is the mean molecular weight for electrons (ions). The expected spectrum

[49] We note that Equations (7) and (8) only apply to optically *thick* dust and that radiation will continue to get reprocessed to IR wavelengths by optically thin dust beyond the maximum dust sublimation radius (J.-Y. Li et al. 2025; S. Tuna et al. 2025). This effect likely contributed to the >30-day NIR excess observed in AT 2018cow, which was not well fit by the opaque dust models explored by S. Tuna et al. (2025).

scales as $L_\nu \propto \nu^{\frac{4s-6}{3s-2}}$ for $s > 1$ (R. Margutti et al. 2019, their Equation (6)). We report below the entire L_ν expression for completeness:

$$L_\nu = \frac{8\pi}{\kappa_{\rm es} c^2} k_B (s-1) f \left(\frac{0.018 \kappa_{\rm es}}{m_p^2 (s-1)} \right)^{\frac{s+1}{3s-2}} \mu_e^{\frac{s-4}{3s-2}} \mu_I^{\frac{s+1}{2-3s}} Z^{\frac{2+2s}{3s-2}} \nu^{\frac{4s-6}{3s-2}} T^{\frac{3s-7}{6s-4}} \rho_0^{\frac{5}{3s-2}} r_0^{\frac{5s}{3s-2}} . \quad (10)$$

For $s = 2$, we find the well-known wind-like medium scaling $L_\nu \propto \nu^{1/2}$.

The $L_{\nu,\rm NIR} \propto \nu^{-0.3}$ observed at $\sim$30 days is broadly consistent with an $s \approx 1.3$ medium. For this medium, the observed NIR L_ν requires $\rho_0 \approx 7 \times 10^{-16}\,{\rm g\,cm^{-3}}$ for an assumed $r_0 = 10^{16}\,{\rm cm}$, $T \approx 20,000\,{\rm K}$, $f = 4\pi$ (i.e., for spherical symmetry), and H-dominated composition. The derived density is $\sim 10^4$ times the CSM density inferred from the radio modeling in equipartition. Thus, in this scenario, the radio and NIR emission components are unlikely to originate from the same CSM, and the NIR originates from extended material above the optically emitting medium. With a density profile $\propto r^{-1.3}$, the medium is significantly shallower than a wind-like profile $\rho = \dot{M}/4\pi v_w r^2$ that is expected for constant $\dot{M}/v_w$. For an assumed wind velocity $v_w = 0.2c$ (motivated by the "expansion velocity" of the blackbody; see Figure 5), the density above corresponds to an effective mass-loss rate $\dot{M}_{\rm eff} \approx 80\,M_\odot\,{\rm yr^{-1}}$. If maintained over a 1-month timescale, this value implies a total ejecta mass of $\sim 7\,M_\odot$. For these parameters we calculate $r_{{\rm th},\nu} \approx 2 \times 10^{15}\,{\rm cm}$ at $\nu_{\rm NIR} \equiv 10^{14}\,{\rm Hz}$ at 30 days, which is a factor of $\sim$4 larger than the blackbody radius ($r_{\rm BB} \approx 4 \times 10^{14}\,{\rm cm}$). The mass in the region $r_{\rm BB} < r < 10^{16}\,{\rm cm}$ at 30 days is $\sim 2.5\,M_\odot$, which is similar to the ejecta mass inferred with Equation (1). We note that it is quantitatively unclear whether very large velocities and the presumably high level of ionization are enough to prevent the detection of prominent lines from this material above the optical photosphere, and we leave the detailed investigation of this aspect to future work.

P. Charalampopoulos et al. (2025) find that this model can well explain the optical-to-NIR emission in AT 2018cow using a wind-like medium scaling for L_ν. They infer at early times ($\delta t < 10$ days) $\dot{M} \approx 60\,M_\odot\,{\rm yr^{-1}}$ and at late times $\dot{M} \approx 22\,M_\odot\,{\rm yr^{-1}}$, with $\dot{M}(t) \propto t^{-1.8}$. Over the 15-day evolution of AT 2018cow, P. Charalampopoulos et al. (2025) estimate the outflow total mass to be $\sim 5.7\,M_\odot$. These parameters are similar to our inferences for AT 2024wpp.

We end with two considerations. First, neither the dust echo model nor the free–free opacity effect model provides a natural explanation for $L_{\rm X}/L_{\rm NIR} \approx 0.5$ for both AT 2018cow and AT 2024wpp, or for the constancy of this ratio throughout the evolution of AT 2018cow (Figure 9). Observations of a larger sample of LFBOTs that extend to the NIR will clarify whether this is a peculiarity of the two events known or a failure of current models. Interestingly, we note that the LFBOT-like transient AT 2024puz also exhibits an NIR excess that was interpreted in the context of both of these models (J. J. Somalwar et al. 2025).

Second, as inferred for AT 2018cow by R. Margutti et al. (2019), for very steep density profiles $s \gg 1$, Equation (10) asymptotically converges to $L_\nu \propto \nu^{4/3}$. This is not dissimilar from the measured slope of the early optical–UV spectrum of AT 2024wpp at $\delta t \approx 6$ days ($L_\nu \propto \nu^{1.3}$), implying that the *optical* continuum is formed in a medium with a steep density gradient, as in AT 2018cow. This is important, since the steepness of the optical continuum-forming medium is a key physical ingredient that we identified in Section 4 to obtain featureless spectra. We note that this last inference is independent of the explanation of the NIR excess.

7. Discussion

7.1. Comparison of AT 2024wpp with Other Transients

In the previous sections we have compared AT 2024wpp with "classical," "cow-like" LFBOTs. Here we expand our comparisons to more broadly include classes of transients that share some aspects of LFBOT phenomenology (in particular, fast-evolving luminous transients and TDEs).

Fast-evolving Luminous Transients. AT 2024puz (J. J. Somalwar et al. 2025) is a peculiar transient with similar properties to both LFBOTs and TDEs (e.g., persistent blue colors, luminous optical emission $L_{\rm pk} \approx 10^{44.8}\,{\rm erg\,s^{-1}}$, featureless spectra, bright and highly variable X-ray emission $L_{\rm X} \approx 10^{44.1}\,{\rm erg\,s^{-1}}$, NIR excess emission above a blackbody), but the UV–optical light curve evolves on an intermediate timescale (10-day rise time, $\sim$20-day evolution timescale; slow for LFBOTs, fast for TDEs). J. J. Somalwar et al. (2025) interpret this object as a slowly evolving LFBOT. The discovery of it points to a continuum of phenomena between LFBOTs and TDEs and suggests that future LFBOT searches may benefit from including phenomena that evolve on slightly longer timescales (J. J. Somalwar et al. 2025).

Other fast-rising and fading ($\sim$10 days), luminous ($M_{\rm peak} < -20$ mag) transients such as Dougie (J. Vinkó et al. 2015), AT 2022adem (M. Nicholl et al. 2023), and AT 2020bot (A. Y. Q. Ho et al. 2023b; M. Nicholl et al. 2023) may also exist within this LFBOT-to-TDE continuum. Both Dougie and AT 2022adem have hot, blue spectral continua, but while Dougie remains featureless through 30 days, AT 2022adem shows H+He emission beginning from 3 days. These features transition to absorption after 14 days. AT 2020bot may be spectrally different from the former two objects, with broad, weak lines at peak brightness that are distinct from traditional SN features and are not obviously identifiable. All of these transients exhibit much faster cooling of their optical–UV emission than typical LFBOTs (especially AT 2020bot), and all occurred in elliptical galaxies with low recent star formation (M. Nicholl et al. 2023), unlike typical (L)FBOT host galaxies (A. Y. Q. Ho et al. 2023b). Additionally, Dougie and AT 2022aedm do not show the luminous X-ray/radio emission that is characteristic of LFBOTs (AT 2020bot was not observed at X-ray or radio wavelengths).

TDEs. There are clear observational analogies between TDEs and LFBOTs. Both classes of objects are characterized by persistently blue optical light curves (S. van Velzen et al. 2011; I. Arcavi et al. 2014; S. van Velzen et al. 2021) and typically only show signatures of H and He in their spectra (S. van Velzen et al. 2021; E. Hammerstein et al. 2023; Y. Yao et al. 2023). The potentially connected subclasses of featureless and jetted TDEs both have persistent featureless optical spectra (I. Andreoni et al. 2023; E. Hammerstein et al. 2023; Y. Yao et al. 2023). As discussed in Section 4, featurelessness can be attributed to a combination of a steep density profile limiting the size of the line formation region, large expansion velocities leading to extreme line broadening, and high ionization of the ejecta.

By analogy with TDE literature (e.g., J. Guillochon et al. 2014; N. Roth et al. 2016), we lean toward the last two explanations for the featurelessness of AT 2024wpp and LFBOTs. We posit the presence of a reprocessing envelope (as in some models of TDEs) but remain agnostic about the astrophysical origin (A. Loeb & A. Ulmer 1997; B. D. Metzger 2022b). TDEs are typically considered nuclear transients involving a supermassive BH (SMBH; S. van Velzen et al. 2019; S. van Velzen et al. 2021; E. Hammerstein et al. 2023; Y. Yao et al. 2023; though recently an off-nuclear SMBH TDE was discovered—see Y. Yao et al. 2025). Most LFBOTs (including AT 2024wpp) are decidedly off-nuclear transients (A. A. Chrimes et al. 2024b); thus, a TDE-like interpretation likely requires an IMBH or stellar-mass BH (or NS). Along with LFBOTs, TDEs are the only other transients known to have late-time X-ray/UV plateaus (A. Mummery et al. 2024) as observed for AT 2018cow (N.-C. Sun et al. 2022; Y. Chen et al. 2023a, 2023b; A. Inkenhaag et al. 2023; N.-C. Sun et al. 2023; G. Migliori et al. 2024). For both classes of transients, this late-time emission is attributed to an accretion disk, but as LFBOTs involve much less massive compact objects, their accretion rate is likely (highly) super-Eddington, which is not always true in TDEs. Thus, LFBOTs may allow us to probe objects with much higher accretion rates than typical TDEs.

7.2. LFBOT Models

AT 2024wpp radiated an extreme $\sim 10^{51}$ erg over the first $\sim$45 days, surpassing AT 2018cow in the same time period, and we thus rule out ordinary neutrino-driven ^{56}Ni-powered core-collapse SNe as the only power source for LFBOT phenomena. Below, we discuss three main physical models for LFBOTs.

(i) D. K. Khatami & D. N. Kasen (2024) propose that LFBOT UVOIR light curves can be modeled as SNe that explode within dense CSM shells, leading to a shock-breakout flash that produces the initial fast rise to peak emission and a subsequent shock-cooling tail. As the blackbody temperature of AT 2024wpp does not cool beyond $\sim$18,000 K (for $\delta t \lesssim 55$ rest-frame days; see Figure 5), we note that this pure CSM interaction interpretation would require very long-lived, continuous interaction to maintain such temperatures. Additionally, the inferred blackbody expansion velocities of up to $0.3c$ imply a compact-object power source with a large enough gravitational well to be able to launch such fast outflows. But instead, if the outflows are interacting with a preexisting CSM, the inferred velocity (dR/dt) is reduced to (few $\times$ 10^{-2} to 10^{-3})c. However, more importantly, the CSM interaction model struggles to reproduce the X-ray nonthermal spectrum and rapid variability discussed in Paper II. Thus, we disfavor a pure CSM interaction model for LFBOT phenomena, though we note that CSM interaction could play a role in addition to accretion onto a compact object (e.g., to produce the observed radio emission). We thus consider two alternative models that involve compact-object accretion.

(ii) Following D. Tsuna & W. Lu (2025), we consider the production of an LFBOT via a stripped-envelope SN (SN Ibc) that produces a compact object with a kick that is fortuitously aligned such that the compact object can disrupt and accrete its main-sequence companion at a super-Eddington rate. The LFBOT is a consequence of the accretion and occurs with some time delay after the SN. Generally, if the compact object is a BH, super-Eddington accretion could provide the 10^{51} erg radiated by AT 2024wpp (an NS falls just short of producing the energetics of AT 2024wpp but could be enough for AT 2018cow; see D. Tsuna & W. Lu 2025, their Equations (16) and 37) and generate LFBOT-inferred asymmetric geometry and multicomponent outflows. D. Tsuna & W. Lu (2025) find that their models are able to reproduce rates consistent with LFBOT observational rates, as well as typical LFBOT features, including the fast ($\sim 0.2c$) outflows originating from the super-Eddington accretion winds, spectra that evolve from featureless to presenting weak H and He lines at $\sim$20 days with widths of a few $\times$ 10^3 km s^{-1} and small $L_{\mathrm{H}\alpha}/L_{\mathrm{rad}} < 1\%$, the evolution of the ratio $L_{\mathrm{X}}/L_{\mathrm{UVOIR}}$ from $<<1$ to $\sim$1 over the same timescale due to X-ray ionization of the ejecta, and the steep radio-inferred CSM density profile at $R > 10^{16}$ cm likely due to the He star's mass loss within the past few centuries before explosion. If the CSM is dense enough, it could naturally produce a dust echo emitting the observed NIR excess as discussed in Section 6.1, though free–free opacity effects (Section 6.2) could also produce this emission component.

Observationally, the challenge for this model is avoiding the detection of the SN. If there were an SN Ibc that occurred just before the LFBOT, the SN would have to be significantly underluminous with a short delay time before the LFBOT in order for the SN to remain undetected. Nothing suggesting the presence of an SN has been detected in an LFBOT thus far. The SN may also dominate the light curve once the FBOT emission fades significantly, though observations of AT 2018cow at 2–4 yr after discovery showed a bright ($L \approx 10^{39}$ erg s^{-1}), blue (F336W $-$ F555W $= -1.3$ mag) source interpreted as a remnant accretion disk around a BH (N.-C. Sun et al. 2022, 2023; Y. Chen et al. 2023b), which could potentially prevent detection of the SN light-curve component. With our 40-day bolometric light curve for AT 2024wpp, we find that an SN 1998bw–like object could account for $\sim$50% of the emission by day 30 ($\gtrsim$80% by day 40). However, as the SN emission becomes more dominant, we would also expect typical SN Ibc spectral features to be produced (e.g., Ca, O, similar to the SN 2025kg–like events), which have yet to be observed in LFBOTs.

(iii) B. D. Metzger (2022a) model LFBOTs as emission from the tidal disruption of a W-R star with a compact-object binary companion (either NS or stellar-mass BH) and subsequent super-Eddington accretion. The optical light curve is produced by some combination of reprocessed X-rays produced by the central accretion disk and shock interaction between the W-R ejecta and CSM from prior mass-loss events. Observed X-rays would consist of the fraction that were not reprocessed by the intervening material. This model broadly produces phenomena consistent with AT 2018cow, and thus AT 2024wpp, including a viscous accretion timescale of less than a few days, matching with LFBOT peak timescales; energy budget from super-Eddington accretion of $\sim 10^{51}$ erg; generation of both fast polar ($0.1c$) and slow equatorial (few $\times$ 10^4 km s^{-1}) outflows; $L_{\mathrm{engine}} \propto t^{-2.1}$ for an accretion efficiency of $\eta \approx 0.01$ (reasonable for super-Eddington accretion onto a magnetar or BH), which is slightly shallower than observed in AT 2024wpp ($L_{\mathrm{engine}} \propto t^{-3.4}$; see Figure 8) but more consistent with the L_{engine} evolution of AT 2018cow ($\propto t^{-1.9}$; R. Margutti et al. 2019); low ^{56}Ni abundance ($<10^{-2}\,M_{\odot}$) in the disk outflows consistent with AT 2018cow light-curve modeling (D. A. Perley et al. 2019); rough agreement with the observed optical light curve of AT 2018cow, where the early-time emission is reprocessed X-rays and the resulting X-ray luminosity is suppressed owing

to this absorption causing $L_X/L_{UVOIR} < 1$ until $\tau_X \approx 1$ at $\sim$20 days; and a density of $n \approx 10^5\,cm^{-3}$ combined with a steepening of the density profile from $n \propto r^{-2}$ to $\propto r^{-3}$ at $r \approx 10^{16}$ cm in the remnant circumbinary disk, which is produced by W-R mass loss prior to the explosion and is consistent with radio-inferred densities. CSM formed by this mass loss would provide a natural environment for an NIR dust echo to be produced as discussed in Section 6.1. B. D. Metzger (2022a) further predict a potential flattening of the light curve at late times ($\gtrsim$100 days) due to the compact-object accretion rate approaching the Eddington limit, which was observed in AT 2018cow (N.-C. Sun et al. 2022, 2023; Y. Chen et al. 2023b). Assuming that AT 2024wpp had similar luminosities and light-curve evolution to AT 2018cow (see Figure 4 of Y. Chen et al. 2023b), the Hubble Space Telescope (HST) could have observed such behavior up to $\sim$100 days.

We note that B. D. Metzger (2022a) disfavor an IMBH ($\gtrsim 10^3\,M_\odot$) central compact object owing to the need for dense CSM. From analysis of the viscous spreading of the disk over 2–4 yr, an IMBH TDE origin for AT 2018cow would require a very small companion (see G. Migliori et al. 2024), while a W-R and stellar-mass BH system more naturally produces the observed emitting region size. Modeling of the late-time emission from future LFBOTs, as well as host galaxy studies, will be able to help constrain the underlying compact object.

Further, this model predicts an LFBOT continuum where slower-evolving transients reach higher luminosities (see Figure 3 of B. D. Metzger 2022a), as increasing the system mass (i.e., M_{BH} and the W-R mass $M_{W\text{-}R}$) can lead to both a longer viscous timescale and peak accretion rate, thus flattening and increasing the peak of the light curve. This continuum is broadly consistent with the properties of AT 2024wpp (and AT 2024puz) compared to other LFBOTs.

To conclude this subsection, overall the models that are the most successful in accounting for the panchromatic properties of LFBOTs share the common ingredient of a central engine in the form of a super-Eddington accretion disk around a compact object and invoke shocks between outflows launched by the accretion disk and/or between disk outflows and preexisting CSM as a way to thermalize some of the energy released by the central engine. At the time of writing, the astrophysical origin and nature of the compact object are open questions.

8. Summary and Conclusions

We have presented an extensive UVOIR photometric (Figure 1) and spectroscopic (Figures 2 and 3) observational campaign for the third LFBOT to be well sampled in this wavelength range during the time period $\delta t = 0.1$–97 days. We summarize our findings as follows:

1. AT 2024wpp is the most luminous LFBOT discovered to date (both at UV wavelengths and bolometrically; see Figure 4), reaching $L_{pk} \approx (2-4) \times 10^{45}\,erg\,s^{-1}$ at peak (which is $\sim$5–10 times larger than the prototypical event of this class, AT 2018cow). The UV–optical spectrum is dominated by a thermal continuum at all times (Figure 2). From our blackbody fits (Figure 5), we infer $T > 30{,}000$ K and blackbody "expansion velocities" of $0.2c$–$0.3c$ at peak—slightly larger than (but comparable to) the mildly relativistic expansion of the optical photosphere inferred for AT 2018cow. Similarly to AT 2018cow, AT 2024wpp maintains a high temperature ($\gtrsim$20,000 K) throughout our monitoring. We infer an initial $R_{BB} \approx 2 \times 10^{15}$ cm. Unlike ordinary SNe, R_{BB} shows a brief phase of expansion in the first few days before decreasing monotonically. The post-peak bolometric luminosity shows rapid fading $\propto t^{-3.4}$.
2. The rise time t_{rise} of AT 2024wpp is among the longest of known classical LFBOTs (Figure 4). Assuming that $t_{rise} = 4$ days reflects the diffusion timescale of radiation from a central source (we note this is an upper limit), we infer an ejecta mass $M_{ej} \lesssim 1$–$2\,M_\odot$, which is larger than inferred for AT 2018cow but consistent with the longer rise time of AT 2024wpp to peak while allowing for a similar mildly relativistic initial blackbody expansion velocity.
3. Over the first $\sim$45 days, AT 2024wpp radiated $>10^{51}$ erg (Table 1), more than an order of magnitude above that radiated by AT 2018cow in a similar timescale, and a value only matched by the most luminous stellar explosions. The large E_{rad} rules out ordinary neutrino-driven SNe and requires additional sources of energy. Among these, we favor super-Eddington accretion-powered systems harboring a compact object (most likely a BH). Similarly to the other two LFBOTs with existing spectral sequences (CSS161010, C. P. Gutiérrez et al. 2024; AT 2018cow, R. Margutti et al. 2019; D. A. Perley et al. 2019), the spectra of AT 2024wpp are entirely featureless for weeks post-discovery (Figure 2). This is a hallmark observational feature of LFBOTs that sets them apart from SNe. Interestingly, this observational trait is also seen in the new class of "featureless TDEs" (I. Andreoni et al. 2023; E. Hammerstein et al. 2023; Y. Yao et al. 2023), with which LFBOTs share the presence of a central source of high-energy emission. By analogy with featureless TDEs, we suggest that featureless spectra might result from persistent ionization of the fast-expanding ejecta.
4. At $\delta t > 35$ days, we confidently detect faint (EW $\lesssim 10$ Å; Figure 11) spectral features of H and He with two kinematically separate velocity components centered at 0 and $-6400\,km\,s^{-1}$ with FWHM $\approx 2000\,km\,s^{-1}$ (Figure 6). A prominently blueshifted component was detected before in CSS 161010 (C. P. Gutiérrez et al. 2024; Figure 7). The line profiles indicate a clear deviation from spherical symmetry. We note that, as in AT 2018cow, the spectral features emerge when $L_X \approx L_{UVOIR}$ (Figure 9).
5. These line profiles imply the presence of multiple outflow components—namely, one that is fast and polar, and another that is slower and equatorial. Super-Eddington accretion disks provide a natural explanation for this structure (S. Yoshioka et al. 2024).
6. While overall the UV–optical SED at each epoch is well fit by a blackbody spectrum, between 20 and 30 days we measure an NIR excess of emission, with a power-law spectrum $F_{\nu,NIR} \propto \nu^{-0.3}$ at 30 days (Figure 6). The presence of NIR excess emission is similar to AT 2018cow (R. Margutti et al. 2019; D. A. Perley et al. 2019; Y. Chen et al. 2023a) and AT 2024puz (J. J. Somalwar et al. 2025). The extrapolation of the radio SED of AT 2024wpp to NIR wavelengths

significantly underpredicts the observed flux, implying that the NIR is a distinct emission component.

7. We consider two models to explain the NIR excess: (i) reprocessing of early UV emission by preexisting dust with density $n_0 \approx 4 \times 10^7\,\mathrm{cm}^{-3}$ at $r_0 = 10^{16}\,\mathrm{cm}$ (Section 6.1; following B. D. Metzger & D. A. Perley 2023; S. Tuna et al. 2025), which is consistent with the radio-inferred density from Paper II ($\sim 10^5\,\mathrm{cm}^{-3}$) with large deviation from equipartition; and (ii) free–free scattering occurring in the extended medium above the optical photosphere (Section 6.2; following N. Roth et al. 2016; W. Lu & C. Bonnerot 2020; P. Charalampopoulos et al. 2025; J. J. Somalwar et al. 2025) with density profile $\rho(r) = \rho_0(r_0/r)^{1.3}$. Both models are able to produce the observed $L_{\mathrm{NIR}} = (1.9 \pm 0.3) \times 10^{41}\,\mathrm{erg\,s}^{-1}$ at the time of appearance (30 days). The free–free model requires a density $\rho_0 \approx 7 \times 10^{-16}\,\mathrm{g\,cm}^{-3}$ at $r_0 \approx 10^{16}\,\mathrm{cm}$, which is $\sim 10^4$ times the radio-derived CSM density; thus, in this model we would expect the NIR to originate from CSM separate from the radio-emitting region. However, neither model provides a natural explanation for the roughly constant soft-X-ray-to-NIR luminosity ratio of $L_{\mathrm{X}}/L_{\mathrm{NIR}} \approx 0.5$ (Figure 9).

While the presence of a compact-object central engine is a feature of LFBOT models that successfully reproduce LFBOT phenomenology across the electromagnetic spectrum, the nature of this object is unknown. Circumstantial evidence such as the extreme radiated energy of AT 2024wpp ($E_{rad} \approx 10^{51}\,\mathrm{erg}$) and mildly relativistic velocities inferred in LFBOT radio and optical emission suggests stellar-mass BHs, which would make LFBOTs highly super-Eddington and thus valuable probes of this accretion regime. Progress relies on increasing the small sample of well-studied objects.

As LFBOTs are extremely UV-luminous transients, future UV missions such as ULTRASAT (I. Sagiv et al. 2014) and UVEX (S. R. Kulkarni et al. 2021) will be instrumental for discovering and characterizing these rare transients out to larger volumes and at earlier times. Tens of LFBOTs per year will be discovered by these surveys. Discovering more LFBOTs pre-peak will also allow better sampling of color evolution from pre- to post-rise, potentially revealing the initial reddened colors indicative of sublimation of dusty CSM predicted by B. D. Metzger & D. A. Perley (2023). At the same time, on the follow-up side, higher-cadence NIR monitoring coordinated with X-ray observations to later epochs is also needed to understand whether the X-ray/NIR correlation with time observed in AT 2018cow (Figure 5 of Y. Chen et al. 2023a) is distinctive to LFBOTs and thus requires a model that connects the two emission components. Mid-IR spectroscopy with JWST would also better constrain the SED peak of the observed NIR excess and simultaneously be sensitive to dust features (e.g., the $\sim 9\,\mu$m feature indicating silicate dust composition), which would aid in constraining the progenitor environment. We conclude by emphasizing that only two LFBOTs (three if including AT 2024puz) to date have extensive multiwavelength datasets; thus, future observations are required to probe the diversity of this class and put meaningful population-level constraints on the intrinsic nature of these intriguing objects.

Acknowledgments

Some of the data presented herein were obtained at Keck Observatory, which is a private 501(c)3 nonprofit organization operated as a scientific partnership among the California Institute of Technology, the University of California, and the National Aeronautics and Space Administration (NASA). The Observatory was made possible by the generous financial support of the W. M. Keck Foundation.

The authors wish to recognize and acknowledge the very significant cultural role and reverence that the summit of Maunakea has always had within the Native Hawaiian community. We are most fortunate to have the opportunity to conduct observations from this mountain.

Some of the LRIS data presented in this work were the result of cooperative data-sharing agreements between the classical and ToO programs of our group with another Keck ToO proposal (Keck 2024B proposal U042; PI: S. Valenti) and classical observers (D. Perley and I. Caiazzo).

Observations used in this work were obtained in part at the international Gemini Observatory, a program of NSF's NOIRLab, which is managed by the Association of Universities for Research in Astronomy (AURA, Inc.) under a cooperative agreement with the US National Science Foundation (NSF) on behalf of the Gemini Observatory partnership: the NSF (United States), National Research Council (Canada), Agencia Nacional de Investigación y Desarrollo (Chile), Ministerio de Ciencia, Tecnología e Innovación (Argentina), Ministério da Ciência, Tecnologia, Inovações e Comunicações (Brazil), and Korea Astronomy and Space Science Institute (Republic of Korea).

A major upgrade of the Kast spectrograph on the Shane 3 m telescope at Lick Observatory, led by Brad Holden, was made possible through gifts from the Heising-Simons Foundation, William and Marina Kast, and the University of California Observatories. Research at Lick Observatory is partially supported by a generous gift from Google.

These results made use of the Lowell Discovery Telescope (LDT) at Lowell Observatory. Lowell is a private, nonprofit institution dedicated to astrophysical research and public appreciation of astronomy and operates the LDT in partnership with Boston University, the University of Maryland, the University of Toledo, Northern Arizona University, and Yale University. The upgrade of the DeVeny optical spectrograph has been funded by a generous grant from John and Ginger Giovale and by a grant from the Mt. Cuba Astronomical Foundation.

The Southern African Large Telescope (SALT) observations presented here were taken under Rutgers University program 2024-1-MLT-003 (PI: S. W. Jha). Research on astrophysical transients at Rutgers University is supported by NSF grant AST-2407567.

This research has made use of data and software provided by the High Energy Astrophysics Science Archive Research Center (HEASARC), which is a service of the Astrophysics Science Division at NASA/GSFC.

This work has made use of data from the Asteroid Terrestrial-impact Last Alert System (ATLAS) project. The ATLAS project is primarily funded to search for near-Earth objects through NASA grants NN12AR55G, 80NSSC18K0284, and 80NSSC18K1575; by-products of the NEO search include images and catalogs from the survey area. This work was partially funded by Kepler/K2 grant

J1944/80NSSC19K0112, HST GO-15889, and STFC grants ST/T000198/1 and ST/S006109/1. The ATLAS science products have been made possible through the contributions of the University of Hawaii Institute for Astronomy, the Queen's University Belfast, the Space Telescope Science Institute, the South African Astronomical Observatory, and the Millennium Institute of Astrophysics (MAS), Chile.

BLAST makes use of the following software packages: AstroPy(Astropy Collaboration et al. 2018), NumPy (C. R. Harris et al. 2020), GHOST (A. Gagliano et al. 2021), PhotUtils (L. Bradley et al. 2024b), Astroquery (A. Ginsburg et al. 2019), HiPS(P. Fernique et al. 2015), DYNESTY(J. S. Speagle 2020), Prospector(B. D. Johnson et al. 2021), sedpy(B. D. Johnson 2021), SVO Filter Profile Service (C. Rodrigo & E. Solano 2020), Healpy(A. Zonca et al. 2019), Python FSPS(B. Johnson et al. 2024), SBI (A. Tejero-Cantero et al. 2020), and SBI++(B. Wang et al. 2023).

R.M. acknowledges support by the National Science Foundation under award No. AST-2224255 and by NASA under grants 80NSSC22K1587, 80NSSC25K7591 and 80NSSC22K0898. A.V.F.'s research group at UC Berkeley acknowledges financial assistance from the Christopher R. Redlich Fund, as well as donations from Gary and Cynthia Bengier, Clark and Sharon Winslow, Alan Eustace and Kathy Kwan, William Draper, Timothy and Melissa Draper, Briggs and Kathleen Wood, Sanford Robertson (W.Z. is a Bengier-Winslow-Eustace Specialist in Astronomy, T.G.B. is a Draper-Wood-Robertson Specialist in Astronomy, Y.Y. was a Bengier-Winslow-Robertson Fellow in Astronomy), and many other donors. N.L. thanks the LSST-DA Data Science Fellowship Program, which is funded by LSST-DA, the Brinson Foundation, the WoodNext Foundation, and the Research Corporation for Science Advancement Foundation; her participation in the program has benefited this work. C.D.K. gratefully acknowledges support from the NSF through grant AST-2432037, from the HST Guest Observer Program through HST-SNAP-17070 and HST-GO-17706, and from JWST Archival Research through JWST-AR-6241 and JWST-AR-5441. G.M. acknowledges financial support from the INAF mini-grant "The high-energy view of jets and transient" (Bando Ricerca Fondamentale INAF 2022).

Facilities: Swift (XRT and UVOT), Keck:I, Keck:II, Shane, LCOGT, ATLAS, Gemini:South, Thacher, SALT, LDT, GALEX.

Software: Astropy (Astropy Collaboration et al. 2013, 2018, 2022), NumPy (C. R. Harris et al. 2020), synphot (STScI Development Team 2018), Matplotlib (J. D. Hunter 2007), photutils (L. Bradley et al. 2024a), HOTPANTS (A. Becker 2015), photpipe (A. Rest et al. 2005), DRAGONS (K. Labrie et al. 2023a, 2023b), SWarp (E. Bertin 2010), DoPhot (P. L. Schechter et al. 1993), UCSC Spectral Pipeline (M. R. Siebert et al. 2020), LPipe (D. A. Perley 2019), PySALT (S. M. Crawford et al. 2010), PypeIt (J. Prochaska et al. 2020; J. X. Prochaska et al. 2020), Astroalign (M. Beroiz et al. 2020).

Appendix A
AT 2023fhn Swift *w*1 photometry

Swift UVOT observed AT 2023fhn beginning at 2023-04-25 08:24:30 ($\delta t = 15.1$ days). We report 20.68 ± 0.08 mag as the non-extinction-corrected $w1$ magnitude. We reduced and corrected this photometry for Galactic extinction using the methods performed for the AT 2024wpp Swift UVOT photometry in Section 2. MW extinction was corrected using $R_V = 3.1$ with the E. L. Fitzpatrick (1999) model with $A_V = 0.078$ mag and $E(B-V) = 0.025$ mag.

In Figure 13, we show the color evolution of AT2024wpp over the first ∼45 days.

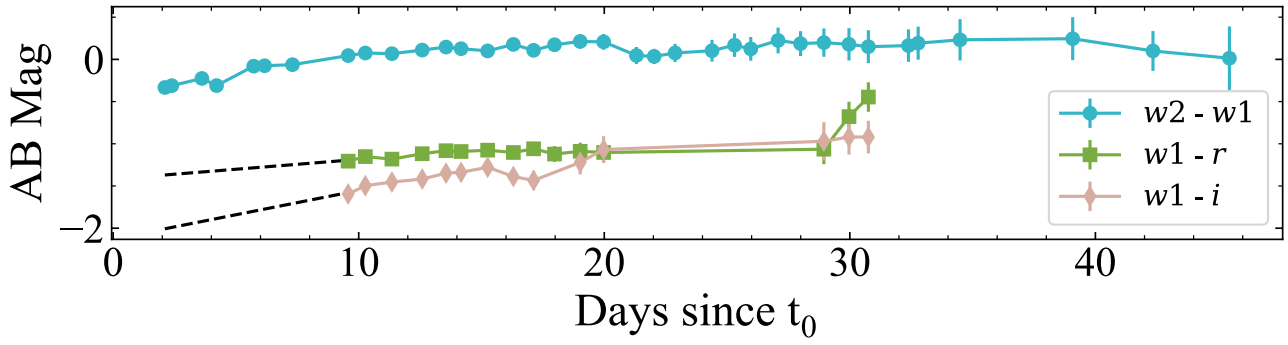

Figure 13. Color evolution of AT 2024wpp. The black dashed lines are extrapolations of the $w1$–r and $w1$–i colors to the beginning of the Swift photometry on day +2, which were used to derive the blackbody temperature and radius fits presented in Figure 5.

Appendix B
Data Tables

In Tables B1, B2, B3, B4, and B5 we provide the details of our observations, which are described in Section 2.

Table B1
Ground-based Optical Photometry (AB mag)

UTC Date	MJD	Phase[a]	Mag	Filter	Mag	Filter	Mag	Filter	Telescope
2024-09-25	60578.44	0.11	20.7 ± 0.3	*g*	⋯	⋯	⋯	⋯	ZTF
2024-09-26	60579.37	1.0	17.46 ± 0.05	*g*	⋯	⋯	⋯	⋯	ZTF
2024-10-02	60585.0	6.7	16.35 ± 0.04	*g*	16.63 ± 0.04	*r*	17.02 ± 0.07	*i*	REM
2024-10-02	60585.9	7.5	16.41 ± 0.05	*g*	16.9 ± 0.2	*r*	17.39 ± 0.06	*i*	LCO
2024-10-03	60586.0	7.7	16.60 ± 0.03	*g*	16.94 ± 0.03	*r*	17.19 ± 0.06	*i*	REM
2024-10-03	60586.4	8.1	⋯	⋯	16.94 ± 0.06	*r*	17.5 ± 0.1	*i*	Supra Solem
2024-10-03	60586.7	8.3	16.61 ± 0.01	*g*	17.01 ± 0.02	*r*	17.50 ± 0.02	*i*	LCO
2024-10-04	60587.3	9.0	16.77 ± 0.02	*g*	17.16 ± 0.02	*r*	17.57 ± 0.04	*i*	Thacher
2024-10-04	60587.4	9.0	⋯	⋯	17.02 ± 0.07	*r*	17.8 ± 0.1	*i*	Supra Solem
2024-10-04	60587.9	9.5	16.87 ± 0.03	*g*	17.27 ± 0.03	*r*	17.67 ± 0.03	*i*	LCO
2024-10-04	60587.9	9.6	⋯	⋯	17.34 ± 0.02	*r*	17.64 ± 0.04	*i*	LCO
2024-10-05	60588.3	10.0	17.07 ± 0.02	*g*	17.36 ± 0.02	*r*	17.68 ± 0.03	*i*	Thacher
2024-10-05	60588.4	10.0	⋯	⋯	17.65 ± 0.08	*r*	17.9 ± 0.2	*i*	Supra Solem
2024-10-05	60588.6	10.2	17.11 ± 0.02	*g*	17.47 ± 0.02	*r*	17.83 ± 0.05	*i*	LCO
2024-10-06	60589.7	11.4	17.43 ± 0.02	*g*	17.79 ± 0.02	*r*	18.01 ± 0.04	*i*	LCO
2024-10-07	60590.9	12.6	17.69 ± 0.04	*g*	17.97 ± 0.05	*r*	18.27 ± 0.06	*i*	LCO
2024-10-09	60592.5	14.1	17.86 ± 0.09	*g*	18.5 ± 0.1	*r*	⋯	⋯	Supra Solem
2024-10-10	60593.2	14.9	18.13 ± 0.03	*g*	18.43 ± 0.04	*r*	18.59 ± 0.05	*i*	LCO
2024-10-10	60593.7	15.4	18.21 ± 0.04	*g*	18.61 ± 0.04	*r*	18.83 ± 0.05	*i*	LCO
2024-10-11	60594.2	15.9	18.4 ± 0.1	*g*	⋯	⋯	⋯	⋯	Thacher
2024-10-11	60594.3	16.0	⋯	⋯	18.6 ± 0.2	*r*	⋯	⋯	Supra Solem
2024-10-12	60595.4	17.1	18.51 ± 0.07	*g*	18.91 ± 0.06	*r*	19.3 ± 0.1	*i*	LCO
2024-10-12	60595.5	17.1	18.5 ± 0.1	*g*	18.9 ± 0.2	*r*	⋯	⋯	Supra Solem
2024-10-13	60596.2	17.9	18.9 ± 0.1	*g*	18.95 ± 0.08	*r*	⋯	⋯	Thacher
2024-10-15	60598.3	19.9	19.19 ± 0.07	*g*	19.47 ± 0.09	*r*	19.4 ± 0.1	*i*	LCO
2024-10-24	60607.2	28.9	20.09 ± 0.06	*g*	20.7 ± 0.1	*r*	20.6 ± 0.2	*i*	LCO
2024-10-25	60608.3	29.9	20.07 ± 0.05	*g*	20.49 ± 0.09	*r*	20.7 ± 0.1	*i*	LCO
2024-10-04	60587.3	9.0	17.57 ± 0.09	*z*	⋯	⋯	⋯	⋯	Thacher
2024-10-05	60588.3	10.0	17.74 ± 0.08	*z*	⋯	⋯	⋯	⋯	Thacher
2024-10-13	60596.2	17.9	19.5 ± 0.2	*z*	⋯	⋯	⋯	⋯	Thacher
2024-09-24	60577.3	-1.0	> 18.3[b]	o	⋯	⋯	⋯	⋯	ATLAS
2024-09-27	60580.0	1.7	17.54 ± 0.03	o	⋯	⋯	⋯	⋯	ATLAS
2024-10-01	60584.9	6.6	16.88 ± 0.02	o	⋯	⋯	⋯	⋯	ATLAS
2024-10-03	60587.0	8.7	17.20 ± 0.02	o	⋯	⋯	⋯	⋯	ATLAS
2024-10-04	60588.0	9.7	17.33 ± 0.02	o	⋯	⋯	⋯	⋯	ATLAS
2024-10-08	60591.5	13.2	18.20 ± 0.04	o	⋯	⋯	⋯	⋯	ATLAS
2024-10-09	60593.0	14.6	18.44 ± 0.06	o	⋯	⋯	⋯	⋯	ATLAS
2024-10-10	60593.1	14.8	18.6 ± 0.2	o	⋯	⋯	⋯	⋯	ATLAS
2024-10-11	60594.6	16.3	18.61 ± 0.06	o	⋯	⋯	⋯	⋯	ATLAS
2024-10-12	60595.9	17.6	19.1 ± 0.2	o	⋯	⋯	⋯	⋯	ATLAS
2024-10-15	60598.4	20.1	19.5 ± 0.2	o	⋯	⋯	⋯	⋯	ATLAS
2024-10-17	60600.1	21.7	18.9 ± 0.3	o	⋯	⋯	⋯	⋯	ATLAS
2024-10-19	60602.3	23.9	19.5 ± 0.3	o	⋯	⋯	⋯	⋯	ATLAS
2024-10-22	60605.3	26.9	> 19.6[b]	o	⋯	⋯	⋯	⋯	ATLAS
2024-10-23	60606.2	27.9	> 19.5[b]	o	⋯	⋯	⋯	⋯	ATLAS
2024-09-28	60581.3	3.0	16.48 ± 0.01	c	⋯	⋯	⋯	⋯	ATLAS
2024-09-29	60582.2	3.9	16.30 ± 0.01	c	⋯	⋯	⋯	⋯	ATLAS
2024-10-03	60586.2	7.9	16.65 ± 0.01	c	⋯	⋯	⋯	⋯	ATLAS
2024-10-10	60593.2	14.9	18.28 ± 0.04	c	⋯	⋯	⋯	⋯	ATLAS
2024-10-23	60606.9	28.5	20.3 ± 0.2	c	⋯	⋯	⋯	⋯	ATLAS
2024-10-24	60608.0	29.6	> 20.1[b]	c	⋯	⋯	⋯	⋯	ATLAS
2024-10-25	60608.0	29.7	> 20.1[b]	c	⋯	⋯	⋯	⋯	ATLAS

Note.
[a] Relative to t_0 (MJD 60578.3).
[b] Upper limit.

Table B2
Swift UVOT Photometry (AB mag)

UTC Date	MJD	Phase[a]	*w*1	*w*2	*m*2	*U*	*B*	*V*
2024-09-27	60580.4	2.1	15.74 ± 0.04	15.52 ± 0.04	⋯	16.01 ± 0.05	16.46 ± 0.06	⋯
2024-09-27	60580.5	2.2	⋯	15.76 ± 0.04	15.49 ± 0.04	6.03 ± 0.05	16.43 ± 0.06	16.9 ± 0.1
2024-09-27	60580.5	2.2	⋯	15.68 ± 0.04	⋯	16.02 ± 0.05	16.45 ± 0.07	⋯
2024-09-27	60580.6	2.3	⋯	15.72 ± 0.04	15.39 ± 0.05	15.99 ± 0.04	16.43 ± 0.06	⋯
2024-09-27	60580.6	2.3	⋯	15.63 ± 0.04	15.42 ± 0.04	16.01 ± 0.05	16.37 ± 0.06	⋯
2024-09-27	60580.7	2.4	15.48 ± 0.04	15.64 ± 0.04	15.39 ± 0.04	15.99 ± 0.04	16.36 ± 0.06	16.8 ± 0.1
2024-09-28	60581.8	3.5	15.29 ± 0.04	⋯	⋯	15.65 ± 0.04	16.04 ± 0.05	⋯
2024-09-28	60581.9	3.6	15.33 ± 0.04	⋯	⋯	⋯	⋯	⋯
2024-09-29	60582.0	3.7	15.32 ± 0.04	15.17 ± 0.04	⋯	15.60 ± 0.04	16.01 ± 0.05	⋯
2024-09-29	60582.4	4.1	15.29 ± 0.04	⋯	⋯	15.52 ± 0.04	15.99 ± 0.06	⋯
2024-09-29	60582.4	4.1	⋯	⋯	⋯	15.56 ± 0.04	⋯	⋯
2024-09-29	60582.5	4.2	15.29 ± 0.04	15.14 ± 0.04	⋯	15.59 ± 0.04	15.98 ± 0.05	⋯
2024-09-30	60583.7	5.4	15.36 ± 0.04	⋯	⋯	15.60 ± 0.04	16.12 ± 0.08	⋯
2024-10-01	60584.0	5.7	15.27 ± 0.04	15.41 ± 0.04	15.42 ± 0.04	15.63 ± 0.05	16.03 ± 0.06	16.5 ± 0.1
2024-10-01	60584.1	5.8	15.31 ± 0.04	15.41 ± 0.05	15.39 ± 0.04	15.63 ± 0.05	15.94 ± 0.07	16.3 ± 0.1
2024-10-01	60584.3	6.0	15.33 ± 0.05	15.42 ± 0.04	⋯	15.67 ± 0.06	16.09 ± 0.08	16.3 ± 0.2
2024-10-01	60584.7	6.4	15.38 ± 0.04	15.47 ± 0.04	15.49 ± 0.04	15.63 ± 0.04	16.11 ± 0.05	16.52 ± 0.09
2024-10-02	60585.6	7.3	15.53 ± 0.04	15.60 ± 0.04	15.64 ± 0.04	15.84 ± 0.04	16.22 ± 0.05	16.66 ± 0.09
2024-10-04	60587.8	9.5	16.03 ± 0.04	16.09 ± 0.04	16.18 ± 0.04	16.26 ± 0.05	16.77 ± 0.06	17.1 ± 0.1
2024-10-05	60588.4	10.1	16.23 ± 0.04	16.23 ± 0.04	16.37 ± 0.04	16.44 ± 0.05	16.88 ± 0.07	17.2 ± 0.1
2024-10-07	60590.4	12.1	16.79 ± 0.05	16.78 ± 0.05	16.95 ± 0.05	16.83 ± 0.06	17.28 ± 0.08	17.7 ± 0.2
2024-10-07	60590.5	12.2	16.80 ± 0.04	16.80 ± 0.04	17.00 ± 0.04	16.88 ± 0.04	17.49 ± 0.06	17.9 ± 0.2
2024-10-07	60590.7	12.4	16.74 ± 0.04	16.84 ± 0.04	16.95 ± 0.04	16.89 ± 0.04	17.37 ± 0.05	17.8 ± 0.1
2024-10-09	60592.5	14.2	17.16 ± 0.05	⋯	⋯	⋯	⋯	⋯
2024-10-10	60593.5	15.2	17.50 ± 0.05	17.45 ± 0.06	17.62 ± 0.05	⋯	⋯	⋯
2024-10-11	60594.4	16.1	⋯	⋯	⋯	18.3 ± 0.2	⋯	⋯
2024-10-11	60594.6	16.3	17.83 ± 0.05	17.69 ± 0.06	17.93 ± 0.05	17.74 ± 0.07	18.3 ± 0.1	⋯
2024-10-12	60595.4	17.1	17.87 ± 0.05	17.82 ± 0.06	17.97 ± 0.05	18.01 ± 0.09	18.2 ± 0.1	⋯
2024-10-13	60596.3	18.0	18.14 ± 0.06	⋯	⋯	⋯	⋯	⋯
2024-10-13	60596.8	18.5	⋯	⋯	⋯	18.3 ± 0.2	⋯	⋯
2024-10-14	60597.3	19.0	18.21 ± 0.06	18.11 ± 0.07	18.40 ± 0.06	18.3 ± 0.1	18.7 ± 0.2	⋯
2024-10-16	60599.6	21.3	18.61 ± 0.07	18.68 ± 0.09	18.76 ± 0.07	18.6 ± 0.1	⋯	⋯
2024-10-17	60600.3	22.0	18.99 ± 0.08	19.1 ± 0.1	19.36 ± 0.09	18.8 ± 0.1	⋯	⋯
2024-10-17	60600.4	22.1	⋯	⋯	⋯	19.0 ± 0.3	⋯	⋯
2024-10-18	60601.2	22.9	18.93 ± 0.07	18.9 ± 0.1	19.04 ± 0.08	18.9 ± 0.1	⋯	⋯
2024-10-19	60602.4	24.1	⋯	⋯	⋯	19.4 ± 0.2	⋯	⋯
2024-10-19	60602.7	24.4	19.22 ± 0.08	19.1 ± 0.1	19.4 ± 0.1	19.2 ± 0.2	⋯	⋯
2024-10-20	60603.5	25.2	⋯	⋯	⋯	19.4 ± 0.4	⋯	⋯
2024-10-20	60603.6	25.3	19.25 ± 0.09	19.2 ± 0.1	19.25 ± 0.09	19.2 ± 0.2	⋯	⋯
2024-10-21	60604.8	26.5	⋯	⋯	⋯	19.2 ± 0.2	⋯	⋯
2024-10-22	60605.4	27.1	19.48 ± 0.09	19.6 ± 0.1	⋯	19.7 ± 0.2	⋯	⋯
2024-10-23	60606.3	28.0	19.7 ± 0.1	19.5 ± 0.1	20.0 ± 0.1	20.1 ± 0.3	⋯	⋯
2024-10-24	60607.1	28.8	19.8 ± 0.1	19.7 ± 0.2	20.0 ± 0.1	19.4 ± 0.2	⋯	⋯
2024-10-24	60607.3	29.0	⋯	⋯	⋯	19.7 ± 0.3	⋯	⋯
2024-10-25	60608.6	30.3	19.9 ± 0.2	19.7 ± 0.1	19.7 ± 0.1	19.4 ± 0.2	⋯	⋯
2024-10-26	60609.0	30.7	19.6 ± 0.1	19.7 ± 0.1	19.9 ± 0.1	19.3 ± 0.2	⋯	⋯
2024-10-27	60610.7	32.4	20.2 ± 0.1	20.1 ± 0.1	⋯	19.9 ± 0.3	⋯	⋯
2024-10-28	60611.1	32.8	20.3 ± 0.1	20.4 ± 0.2	⋯	⋯	⋯	⋯
2024-10-28	60611.9	33.6	⋯	⋯	⋯	20.2 ± 0.3	⋯	⋯
2024-10-29	60612.8	34.5	20.2 ± 0.1	20.1 ± 0.2	20.5 ± 0.1	20.2 ± 0.6	19.4 ± 0.7	⋯
2024-11-06	60620.6	42.3	20.9 ± 0.1	⋯	⋯	⋯	⋯	⋯
2024-11-07	60621.7	43.4	21.0 ± 0.2	21.0 ± 0.1	⋯	20.7 ± 0.3	⋯	⋯
2024-11-09	60623.8	45.5	21.0 ± 0.2	⋯	⋯	⋯	⋯	⋯
2024-11-10	60624.7	46.4	21.3 ± 0.2	⋯	⋯	⋯	⋯	⋯
2024-11-11	60625.7	47.4	20.8 ± 0.2	20.9 ± 0.1	⋯	21.0 ± 0.4	⋯	⋯
2024-11-18	60632.8	54.5	21.3 ± 0.2	⋯	⋯	⋯	⋯	⋯
2024-11-19	60633.7	55.4	21.2 ± 0.3	⋯	⋯	⋯	⋯	⋯
2024-11-22	60636.1	57.8	21.9 ± 0.3	⋯	⋯	⋯	⋯	⋯
2024-11-22	60636.5	58.2	21.3 ± 0.2	21.9 ± 0.2	⋯	⋯	⋯	⋯
2024-11-23	60637.4	59.1	21.6 ± 0.2	⋯	⋯	⋯	⋯	⋯
2024-11-28	60642.3	64.0	21.5 ± 0.2	21.8 ± 0.2	⋯	⋯	⋯	⋯
2024-12-12	60656.3	78.0	22.1 ± 0.3	21.9 ± 0.2	⋯	⋯	⋯	⋯
2024-12-31	60675.2	96.9	22.2 ± 0.3	⋯	⋯	⋯	⋯	⋯

Note.
[a] Relative to t_0 (MJD 60578.3).

Table B3
NIR Photometry (AB mag)

UTC Date	MJD	Phase[a]	Mag	Filter	Mag	Filter	Filter	Mag	Telescope
2024-10-02	60585.0	6.7	> 17.2[b]	J	> 17.7[b]	H	⋯	⋯	REM
2024-10-03	60586.0	7.7	> 17.6[b]	J	⋯	⋯	⋯	⋯	REM
2024-10-12	60595.0	16.7	> 17.5[b]	J	⋯	⋯	⋯	⋯	REM
2024-10-05	60588.3	10.0	18.79 ± 0.04	J	19.21 ± 0.06	H	⋯	⋯	Gemini
2024-10-16	60599.2	20.9	20.47 ± 0.08	J	⋯	⋯	⋯	⋯	Gemini
2024-10-17	60600.2	21.9	20.6 ± 0.1	J	⋯	⋯	⋯	⋯	Gemini
2024-10-25	60608.3	30.0	21.2 ± 0.2	J	21.4 ± 0.1	H	21.0 ± 0.2	K_s	Gemini

Note.
[a] Relative to t_0 (MJD 60578.3).
[b] Upper limit.

Table B4
Optical Spectroscopy

UTC Date	MJD	Phase[a]	Telescope	Instrument	Grating (Blue and Red)	Exposure Time (Blue/Red) (s)
2024-09-29	60582.4	4.1	Shane	Kast	600/4310 and 600/7500	2460/2400
2024-10-01	60584.5	6.2	Shane	Kast	452/3306 and 600/7500	2460/2400
2024-10-01	60584.9	6.6	SALT	RSS	PG0900/5100 and PG0900/5700	1200/1200
2024-10-03	60586.4	8.1	Shane	Kast	452/3306 and 300/7500	1870/1800
2024-10-04	60586.5	9.1	Shane	Kast	600/4310 and 300/7500	1835/1800
2024-10-05	60588.4	10.1	Shane	Kast	600/4310 and 300/7500	1530/1500
2024-10-05	60588.5	10.2	Keck I	LRIS	600/4000 and 400/8500	600/600
2024-10-07	60590.4	12.1	Keck I	LRIS	400/3400 and 400/8500	300/300
2024-10-10	60593.3	15.0	DeVeny	LDT	300/5800	1200
2024-10-11	60594.4	16.1	Shane	Kast	600/4310 and 300/7500	10,980/10,800
2024-10-12	60595.4	17.1	Shane	Kast	452/3306 and 300/7500	3090/3000
2024-10-24	60607.4	29.0	Shane	Kast	452/3306 and 300/7500	4290/4200
2024-10-25	60608.9	30.6	SALT	RSS	PG0900/5100 and PG0900/5700	1200/1200
2024-10-30	60613.4	35.1	Keck I	LRIS	600/4000 and 400/8500	2400/2400
2024-11-08	60622.4	44.1	Keck I	LRIS	600/4000 and 400/8500	4500/4500
2024-11-27	60641.3	63.0	Keck I	LRIS	600/4000 and 400/8500	5400/5250

Note.
[a] Relative to t_0 (MJD 60578.3).

Table B5
NIR Spectroscopy

UTC Date	MJD	Phase[a]	Telescope	Instrument	Filter	Exposure Time (JH/HK) (s)
2024-10-05	60588.3	10.0	Gemini	F2	$JH + HK$	840/840
2024-10-16	60599.2	20.9	Gemini	F2	JH	600
2024-10-17	60600.2	21.9	Gemini	F2	$JH + HK$	960/2040
2024-10-19	60602.5	24.2	Keck II	NIRES	⋯	2200

Note.
[a] Relative to t_0 (MJD 60578.3).

ORCID iDs

Natalie LeBaron https://orcid.org/0000-0002-2249-0595
Raffaella Margutti https://orcid.org/0000-0003-4768-7586
Ryan Chornock https://orcid.org/0000-0002-7706-5668
Nayana A. J. https://orcid.org/0000-0002-8070-5400
Olivia Aspegren https://orcid.org/0000-0001-5674-8403
Wenbin Lu https://orcid.org/0000-0002-1568-7461
Brian D. Metzger https://orcid.org/0000-0002-4670-7509
Daniel Kasen https://orcid.org/0000-0002-5981-1022
Thomas G. Brink https://orcid.org/0000-0001-5955-2502
Sergio Campana https://orcid.org/0000-0001-6278-1576
Paolo D'Avanzo https://orcid.org/0000-0001-7164-1508

Jakob T. Faber https://orcid.org/0000-0001-9855-5781
Matteo Ferro https://orcid.org/0009-0007-5708-7978
Alexei V. Filippenko https://orcid.org/0000-0003-3460-0103
Ryan J. Foley https://orcid.org/0000-0002-2445-5275
Xinze Guo https://orcid.org/0009-0002-9727-8326
Erica Hammerstein https://orcid.org/0000-0002-5698-8703
Saurabh W. Jha https://orcid.org/0000-0001-8738-6011
Charles D. Kilpatrick https://orcid.org/0000-0002-5740-7747
Giulia Migliori https://orcid.org/0000-0003-0216-8053
Dan Milisavljevic https://orcid.org/0000-0002-0763-3885
Kishore C. Patra https://orcid.org/0000-0002-1092-6806
Huei Sears https://orcid.org/0000-0001-8023-4912
Jonathan J. Swift https://orcid.org/0000-0002-9486-818X
Samaporn Tinyanont https://orcid.org/0000-0002-1481-4676
Vikram Ravi https://orcid.org/0000-0002-7252-5485
Yuhan Yao https://orcid.org/0000-0001-6747-8509
Kate D. Alexander https://orcid.org/0000-0002-8297-2473
Prasiddha Arunachalam https://orcid.org/0000-0002-6688-3307
Edo Berger https://orcid.org/0000-0002-9392-9681
Joe S. Bright https://orcid.org/0000-0002-7735-5796
Kyle W. Davis https://orcid.org/0000-0002-5680-4660
Braden Garretson https://orcid.org/0000-0001-6922-8319
Puragra Guhathakurta https://orcid.org/0000-0001-8867-4234
Wynn V. Jacobson-Galán https://orcid.org/0000-0002-3934-2644
D. O. Jones https://orcid.org/0000-0002-6230-0151
Ravjit Kaur https://orcid.org/0009-0005-1871-7856
Tanmoy Laskar https://orcid.org/0000-0003-1792-2338
Michaela Schwab https://orcid.org/0009-0002-5096-1689
Monika D. Soraisam https://orcid.org/0000-0001-6360-992X
Nao Suzuki https://orcid.org/0000-0001-7266-930X
Kirsty Taggart https://orcid.org/0000-0002-5748-4558
Eli Wiston https://orcid.org/0009-0002-4843-2913
Yi Yang https://orcid.org/0000-0002-6535-8500
WeiKang Zheng https://orcid.org/0000-0002-2636-6508

References

Andreoni, I., Coughlin, M. W., Perley, D. A., et al. 2023, Natur, 613, E6
Arcavi, I., Gal-Yam, A., Cenko, S. B., et al. 2012, ApJL, 756, L30
Arcavi, I., Gal-Yam, A., Sullivan, M., et al. 2014, ApJ, 793, 38
Arcavi, I., Wolf, W. M., Howell, D. A., et al. 2016, ApJ, 819, 35
Astropy Collaboration, Price-Whelan, A. M., Lim, P. L., et al. 2022, ApJ, 935, 167
Astropy Collaboration, Price-Whelan, A. M., Sipőcz, B. M., et al. 2018, AJ, 156, 123
Astropy Collaboration, Robitaille, T. P., Tollerud, E. J., et al. 2013, A&A, 558, A33
Becker, A., 2015 HOTPANTS: High Order Transform of PSF ANd Template Subtraction, Astrophysics Source Code Library, ascl:1504.004
Beroiz, M., Cabral, J. B., & Sanchez, B. 2020, A&C, 32, 100384
Bertin, E., 2010 SWarp: Resampling and Co-adding FITS Images Together, Astrophysics Source Code Library, ascl:1010.068
Bradley, L., Sipőcz, B., Robitaille, T., et al. 2024a, astropy/photutils: v1.11.0, Zenodo, doi: 10.5281/zenodo.10671725 10.5281/zenodo.10671725
Bradley, L., Sipőcz, B., Robitaille, T., et al. 2024b, astropy/photutils: v1.13.0, Zenodo, doi: 10.5281/zenodo.12585239 10.5281/zenodo.12585239
Bright, J. S., Margutti, R., Matthews, D., et al. 2022, ApJ, 926, 112
Brown, J. S., Kochanek, C. S., Holoien, T. W. S., et al. 2018, MNRAS, 473, 1130
Brown, P. J., Holland, S. T., Immler, S., et al. 2009, AJ, 137, 4517
Brown, P. J., Roming, P. W. A., Milne, P., et al. 2010, ApJ, 721, 1608
Calderón, D., Pejcha, O., & Duffell, P. C. 2021, MNRAS, 507, 1092
Campana, S., Mangano, V., Blustin, A. J., et al. 2006, Natur, 442, 1008
Charalampopoulos, P., Pursiainen, M., Leloudas, G., et al. 2023, A&A, 673, A95
Charalampopoulos, P., Pursiainen, M., Leloudas, G., et al. 2025, ApJ, 991, 180
Chen, C., & Shen, R.-F. 2022, RAA, 22, 035017
Chen, Y., Drout, M. R., Piro, A. L., et al. 2023a, ApJ, 955, 42
Chen, Y., Drout, M. R., Piro, A. L., et al. 2023b, ApJ, 955, 43
Chrimes, A. A., Coppejans, D. L., Jonker, P. G., et al. 2024a, A&A, 691, A329
Chrimes, A. A., Jonker, P. G., Levan, A. J., et al. 2024b, MNRAS, 527, L47
Coppejans, D. L., Margutti, R., Terreran, G., et al. 2020, ApJL, 895, L23
Covino, S., Zerbi, F. M., Chincarini, G., et al. 2004, AN, 325, 543
Crawford, S. M., Still, M., Schellart, P., et al. 2010, SPIE, 7737, 773725
Crowther, P. A. 2007, ARA&A, 45, 177
Dessart, L., Hillier, D. J., Livne, E., et al. 2011, MNRAS, 414, 2985
Drout, M. R., Chornock, R., Soderberg, A. M., et al. 2014, ApJ, 794, 23
Eikenberry, S., Bandyopadhyay, R., Bennett, J. G., et al. 2012, SPIE, 8446, 84460I
Eikenberry, S. S., Elston, R., Raines, S. N., et al. 2004, SPIE, 5492, 1196
Eyles-Ferris, R. A. J., Jonker, P. G., Levan, A. J., et al. 2025, ApJL, 988, L14
Fernique, P., Allen, M. G., Boch, T., et al. 2015, A&A, 578, A114
Ferrero, P., Kann, D. A., Zeh, A., et al. 2006, A&A, 457, 857
Filippenko, A. V. 1982, PASP, 94, 715
Fitzpatrick, E. L. 1999, PASP, 111, 63
Flewelling, H. 2018, AAS Meeting, 231, 436.01
Foley, R. J., Papenkova, M. S., Swift, B. J., et al. 2003, PASP, 115, 1220
Fulton, M., Chen, T. W., Smartt, S. J., et al. 2024, TNSAN, 206, 1
Gagliano, A., Narayan, G., Engel, A., Carrasco Kind, M. & LSST Dark Energy Science Collaboration 2021, ApJ, 908, 170
Gaia Collaboration, Vallenari, A., Brown, A. G. A., et al. 2023, A&A, 674, A1
Gehrels, N., Chincarini, G., Giommi, P., et al. 2004, ApJ, 611, 1005
Gezari, S., Chornock, R., Lawrence, A., et al. 2015, ApJL, 815, L5
Ginsburg, A., Sipőcz, B. M., Brasseur, C. E., et al. 2019, AJ, 157, 98
Guillochon, J., Manukian, H., & Ramirez-Ruiz, E. 2014, ApJ, 783, 23
Gutiérrez, C. P., Mattila, S., Lundqvist, P., et al. 2024, ApJ, 977, 21
Hammerstein, E., van Velzen, S., Gezari, S., et al. 2023, ApJ, 942, 9
Hamuy, M. 2003, ApJ, 582, 905
Harris, C. R., Millman, K. J., van der Walt, S. J., et al. 2020, Natur, 585, 357
Ho, A. Y. Q., Margalit, B., Bremer, M., et al. 2022, ApJ, 932, 116
Ho, A. Y. Q., Perley, D. A., Chen, P., et al. 2023a, Natur, 623, 927
Ho, A. Y. Q., Perley, D. A., Gal-Yam, A., et al. 2023b, ApJ, 949, 120
Ho, A. Y. Q., Perley, D. A., Kulkarni, S. R., et al. 2020, ApJ, 895, 49
Ho, A. Y. Q., Phinney, E. S., Ravi, V., et al. 2019, ApJ, 871, 73
Ho, A. Y. Q., Srinivasaragavan, G., Perley, D., et al. 2024, TNSAN, 272, 1
Holoien, T. W. S., Kochanek, C. S., Prieto, J. L., et al. 2016, MNRAS, 463, 3813
Holoien, T. W. S., Prieto, J. L., Bersier, D., et al. 2014, MNRAS, 445, 3263
Horne, K. 1986, PASP, 98, 609
Hunter, D. J., Valenti, S., Kotak, R., et al. 2009, A&A, 508, 371
Hunter, J. D. 2007, CSE, 9, 90
Inkenhaag, A., Jonker, P. G., Levan, A. J., et al. 2023, MNRAS, 525, 4042
Inserra, C., Smartt, S. J., Jerkstrand, A., et al. 2013, ApJ, 770, 128
Johnson, B., Foreman-Mackey, D., Sick, J., et al. 2024, dfm/python-fsps: v0.4.7, Zenodo, doi: 10.5281/zenodo.12447779 10.5281/zenodo.12447779
Johnson, B. D. 2021, bd-j/sedpy: sedpy v0.2.0, Zenodo, doi: 10.5281/zenodo.4582723 10.5281/zenodo.4582723
Johnson, B. D., Leja, J., Conroy, C., & Speagle, J. S. 2021, ApJS, 254, 22
Kasen, D., Thomas, R. C., & Nugent, P. 2006, ApJ, 651, 366
Khatami, D. K., & Kasen, D. N. 2024, ApJ, 972, 140
Kiewe, M., Gal-Yam, A., Arcavi, I., et al. 2012, ApJ, 744, 10
Kulkarni, S. R., Harrison, F. A., Grefenstette, B. W., et al. 2021, arXiv:2111.15608
Labrie, K., Simpson, C., Cardenes, R., et al. 2023a, RNAAS, 7, 214
Labrie, K., Simpson, C., Turner, J., et al. 2023b, DRAGONS, v3.1.0, Zenodo, doi: 10.5281/zenodo.7776065 10.5281/zenodo.7776065
Li, J.-Y., Yu, Y.-W., Liu, L.-D., & Xiao, M.-Y. 2025, ApJ, 992, 9
Loeb, A., & Ulmer, A. 1997, ApJ, 489, 573
Lu, W., & Bonnerot, C. 2020, MNRAS, 492, 686
Margalit, B. 2022, ApJ, 933, 238
Margutti, R., Milisavljevic, D., Soderberg, A. M., et al. 2014, ApJ, 780, 21

Margutti, R., Metzger, B. D., Chornock, R., et al. 2019, ApJ, 872, 18
Martin, D. C., Fanson, J., Schiminovich, D., et al. 2005, ApJL, 619, L1
Matsumoto, T., & Piran, T. 2021, MNRAS, 502, 3385
Matthews, D., Margutti, R., Metzger, B. D., et al. 2023, RNAAS, 7, 126
Mazzali, P. A., Deng, J., Pian, E., et al. 2006, ApJ, 645, 1323
Mazzali, P. A., Iwamoto, K., & Nomoto, K. 2000, ApJ, 545, 407
Metzger, B. D. 2022a, ApJ, 932, 84
Metzger, B. D. 2022b, ApJL, 937, L12
Metzger, B. D., & Perley, D. A. 2023, ApJ, 944, 74
Metzger, B. D., Vurm, I., Hascoët, R., & Beloborodov, A. M. 2014, MNRAS, 437, 703
Migliori, G., Margutti, R., Metzger, B. D., et al. 2024, ApJL, 963, L24
Miller, J. S., & Stone, R. 1994, The Kast Double Spectrograph Lick Observatory Tech. Rep. No. 66, Santa Cruz, CA: Lick Observatory
Modjaz, M., Li, W., Butler, N., et al. 2009, ApJ, 702, 226
Mummery, A., van Velzen, S., Nathan, E., et al. 2024, MNRAS, 527, 2452
Nayana, A. J., Margutti, R., Wiston, E., et al. 2025, ApJL, 993, L6
Nicholl, M., Srivastav, S., Fulton, M. D., et al. 2023, ApJL, 954, L28
Ofek, E. O., Ozer, L., Konno, R., et al. 2025, ApJ, 993, 76
Oke, J. B., Cohen, J. G., Carr, M., et al. 1995, PASP, 107, 375
Oke, J. B., & Gunn, J. E. 1983, ApJ, 266, 713
Osterbrock, D. E., & Ferland, G. J. 2006, Astrophysics of Gaseous Nebulae and Active Galactic Nuclei (University Science Books)
Patat, F., Cappellaro, E., Danziger, J., et al. 2001, ApJ, 555, 900
Pellegrino, C., Howell, D. A., Vinkó, J., et al. 2022, ApJ, 926, 125
Perley, D. A. 2019, PASP, 131, 084503
Perley, D. A., Ho, A. Y. Q., Yao, Y., et al. 2021, MNRAS, 508, 5138
Perley, D. A., Mazzali, P. A., Yan, L., et al. 2019, MNRAS, 484, 1031
Perley, D. A., Qin, Y., Rich, R. M., et al. 2024, TNSAN, 280, 1
Pian, E., Mazzali, P. A., Masetti, N., et al. 2006, Natur, 442, 1011
Pignata, G., Stritzinger, M., Soderberg, A., et al. 2011, ApJ, 728, 14
Piro, A. L., & Lu, W. 2020, ApJ, 894, 2
Planck Collaboration, Aghanim, N., Akrami, Y., et al. 2020, A&A, 641, A6
Prentice, S. J., Maguire, K., Smartt, S. J., et al. 2018, ApJL, 865, L3
Prochaska, J., Hennawi, J., Westfall, K., et al. 2020, JOSS, 5, 2308
Prochaska, J. X., Hennawi, J., Cooke, R., et al. 2020, pypeit/PypeIt: Release v1.0.0, Zenodo, doi: 10.5281/zenodo.3743493
Pursiainen, M., Childress, M., Smith, M., et al. 2018, MNRAS, 481, 894
Pursiainen, M., Killestein, T. L., Kuncarayakti, H., et al. 2025, MNRAS, 537, 3298
Quataert, E., Lecoanet, D., & Coughlin, E. R. 2019, MNRAS, 485, L83
Quimby, R. M., Kulkarni, S. R., Kasliwal, M. M., et al. 2011, Natur, 474, 487
Rabinak, I., & Waxman, E. 2011, ApJ, 728, 63
Rastinejad, J. C., Levan, A. J., Jonker, P. G., et al. 2025, ApJL, 988, L13
Rest, A., Garnavich, P. M., Khatami, D., et al. 2018, NatAs, 2, 307
Rest, A., Stubbs, C., Becker, A. C., et al. 2005, ApJ, 634, 1103
Richmond, M. W., van Dyk, S. D., Ho, W., et al. 1996, AJ, 111, 327
Rodrigo, C., & Solano, E. 2020, in XIV.0 Scientific Meeting (virtual) of the Spanish Astronomical Society, 182
Roming, P. W. A., Kennedy, T. E., Mason, K. O., et al. 2005, SSRv, 120, 95
Roth, N., & Kasen, D. 2018, ApJ, 855, 54
Roth, N., Kasen, D., Guillochon, J., & Ramirez-Ruiz, E. 2016, ApJ, 827, 3
Rybicki, G. B., & Lightman, A. P. 1979, Radiative Processes in Astrophysics (Wiley)
Sadowski, A., & Narayan, R. 2015, MNRAS, 453, 3213
Sądowski, A., & Narayan, R. 2016, MNRAS, 456, 3929
Sagiv, I., Gal-Yam, A., Ofek, E. O., et al. 2014, AJ, 147, 79
Schechter, P. L., Mateo, M., & Saha, A. 1993, PASP, 105, 1342
Science Software Branch at STScI, 2012 PyRAF: Python alternative for IRAF, Astrophysics Source Code Library, ascl:1207.011
Short, P., Nicholl, M., Lawrence, A., et al. 2020, MNRAS, 498, 4119
Siebert, M. R., Dimitriadis, G., Polin, A., & Foley, R. J. 2020, ApJL, 900, L27
Silverman, J. M., Foley, R. J., Filippenko, A. V., et al. 2012, MNRAS, 425, 1789
Skrutskie, M. F., Cutri, R. M., Stiening, R., et al. 2006, AJ, 131, 1163
Smith, K. W., Smartt, S. J., Young, D. R., et al. 2020, PASP, 132, 085002
Smith, M. P., Nordsieck, K. H., Burgh, E. B., et al. 2006, SPIE, 6269, 62692A
Smith, N., Mauerhan, J. C., Kasliwal, M. M., & Burgasser, A. J. 2013, MNRAS, 434, 2721
Soderberg, A. M., Kulkarni, S. R., Nakar, E., et al. 2006, Natur, 442, 1014
Somalwar, J. J., Ravi, V., Margutti, R., et al. 2025, ApJ, 995, 32
Speagle, J. S. 2020, MNRAS, 493, 3132
Srinivasaragavan, G. P., Hamidani, H., Schroeder, G., et al. 2025, ApJL, 988, L60
Stritzinger, M., Hamuy, M., Suntzeff, N. B., et al. 2002, AJ, 124, 2100
STScI Development Team., 2018 Synphot: Synthetic photometry using Astropy, Astrophysics Source Code Library, ascl:1811.001
Sun, H., Li, W.-X., Liu, L.-D., et al. 2025, NatAs, 9, 1073
Sun, N.-C., Maund, J. R., Crowther, P. A., & Liu, L.-D. 2022, MNRAS, 512, L66
Sun, N.-C., Maund, J. R., Shao, Y., & Janiak, I. A. 2023, MNRAS, 519, 3785
Swift, J. J., Andersen, K., Arculli, T., et al. 2022, PASP, 134, 035005
Tanaka, M., Tominaga, N., Morokuma, T., et al. 2016, ApJ, 819, 5
Taubenberger, S., Pastorello, A., Mazzali, P. A., et al. 2006, MNRAS, 371, 1459
Tejero-Cantero, A., Boelts, J., Deistler, M., et al. 2020, JOSS, 5, 2505
Tinyanont, S., Foley, R. J., Taggart, K., et al. 2024, PASP, 136, 014201
Tonry, J. L., Denneau, L., Heinze, A. N., et al. 2018, PASP, 130, 064505
Tsuna, D., & Lu, W. 2025, ApJ, 986, 84
Tuna, S., Metzger, B. D., Jiang, Y.-F., & White, C. J. 2025, ApJ, 989, 17
Uno, K., & Maeda, K. 2020, ApJ, 897, 156
Valenti, S., Benetti, S., Cappellaro, E., et al. 2008, MNRAS, 383, 1485
Valenti, S., Fraser, M., Benetti, S., et al. 2011, MNRAS, 416, 3138
van Baal, B. F. A., Jerkstrand, A., Wongwathanarat, A., & Janka, H.-T. 2023, MNRAS, 523, 954
van Dalen, J. N. D., Levan, A. J., Jonker, P. G., et al. 2025, ApJL, 982, L47
van Velzen, S., Farrar, G. R., Gezari, S., et al. 2011, ApJ, 741, 73
van Velzen, S., Gezari, S., Cenko, S. B., et al. 2019, ApJ, 872, 198
van Velzen, S., Gezari, S., Hammerstein, E., et al. 2021, ApJ, 908, 4
Vinkó, J., Yuan, F., Quimby, R. M., et al. 2015, ApJ, 798, 12
Vurm, I., & Metzger, B. D. 2021, ApJ, 917, 77
Wang, B., Leja, J., Villar, V. A., Speagle, J. S., et al. 2023, ApJL, 952, L10
Wang, T.-G., Zhou, H.-Y., Wang, L.-F., Lu, H.-L., & Xu, D. 2011, ApJ, 740, 85
Wilson, J. C., Henderson, C. P., Herter, T. L., et al. 2004, SPIE, 5492, 1295
Wright, A. E., & Barlow, M. J. 1975, MNRAS, 170, 41
Yao, Y., Chornock, R., Ward, C., et al. 2025, ApJL, 985, L48
Yao, Y., Ho, A. Y. Q., Medvedev, P., et al. 2022, ApJ, 934, 104
Yao, Y., Ravi, V., Gezari, S., et al. 2023, ApJL, 955, L6
Yaron, O., & Gal-Yam, A. 2012, PASP, 124, 668
Yoshii, Y., Tomita, H., Kobayashi, Y., et al. 2003, ApJ, 592, 467
Yoshioka, S., Mineshige, S., Ohsuga, K., Kawashima, T., & Kitaki, T. 2024, PASJ, 76, 1015
Zerbi, R. M., Chincarini, G., Ghisellini, G., et al. 2001, AN, 322, 275
Zonca, A., Singer, L., Lenz, D., et al. 2019, JOSS, 4, 1298